Università
degli Studi
di Padova

Master Thesis in Electrical Engineering

Design and optimization of a 9-phase induction machine

Master Candidate

Riccardo Gava
Student ID 2020329

Supervisor

Prof. Nicola Bianchi
Univeristy of Padova

Co-supervisors

Univ.-Prof. Dr.-Ing. Hans-Georg Herzog
Technical University of Munich

Dr.-Ing. Jörg Kammermann
Technical University of Munich

Academic Year 2022/2023

To those who kept my hopes, my spirit, and myself alive during the last months.

Abstract

The intense growth of electric transportation demands new standards in electric systems' reliability and fault tolerance. Alternative solutions to the standard 3-phase machines have been studied in literature to ensure these characteristics. It has been observable that multi-phase machines can provide reduced power per phase, lower torque pulsation, higher reliability, and power density.

This thesis aims to develop a 9-phase induction motor (IM) as an alternative to the already studied machines based on permanent magnets. After some initial considerations on multi-phase systems and the best winding layout, a first design of the 11 kVA IM is proposed, based on the given design specification and criteria. In the following chapter, optimization through a genetic algorithm is performed to maximize the motor's performance and characteristics such as efficiency, reliability, and weight/dimensions. A rated torque of $T = 28.5$Nm and an efficiency $\eta = 89.9\%$ are obtained.
Finally, a Finite-Element-Analysis (FEA) is executed to gain more detailed knowledge about the optimized machine and it is compared to the results of analytical calculations with optimum outcome.

Contents

List of Figures

List of Tables

1 Motivation of work

The ongoing intense electrification of transportation both on the road and in the air is a hot topic of the present day. This phenomenon naturally demands improving reliability and fault-tolerance of the electric drives in these new applications, such as aircraft, automotive, etc.
In order to achieve these higher standards structural and functional redundancy is commonly used. Thanks to the development of power electronics, the redundancy can translated into multi-phase systems; their characteristics and advantages will presented and deeply explained in the following chapter.
As stated in [12], the higher the number of phases the better the is the overall reliability. Simply, a multi-phase system can handle one or more phase failures and still provide the required performances 2.2.

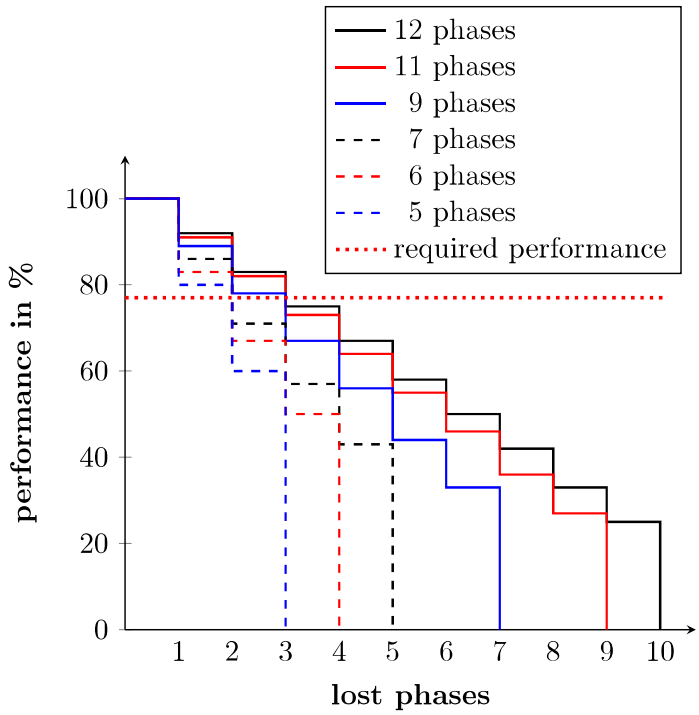

Figure 1.1 – Comparison of different numbers of phases considering the remaining system performance over the number of lost phases [13]

The aim of this work is to study, design, and present the first prototype of a multi-phase induction motor for a test bench. The initial number of phases for the IM is set to $m = 9$. This could also be a valid alternative to the already studied 9-phase synchronous motor [22],

considering IMs do not present permanent magnets, often rare and expensive materials, so they are usually adopted for cheaper and less high-performance applications.

2 Multi-phase winding design

One of the first choices regarding the design of an electrical machine is the winding layout as well as the number of poles and slots, consequently. In this chapter, after a short description of different types of winding and multi-phase systems, a winding layout will be chosen and designed. Finally, the generated magneto-motive force is examined with Fourier analysis.

2.1 Distributed and concentrated winding

Electrical machines can present different types of winding layouts based on the number of phases m, number of poles pairs p, and number of stator slots Q. Winding characteristics can be described using the number of slots per pole and phase, defined as follow:

$$q = \frac{Q}{2p\ m}. \tag{2.1}$$

Since all numbers in the fraction are integers, q must be a rational number. We can have a concentrated or tooth-coil winding if $q < 1$, or a distributed one for $q \geqslant 1$. Distributed winding can then be subdivided into fractional-slot winding if $q \in \mathbb{Q}$ or integer-slot winding if $q \in \mathbb{N}$.

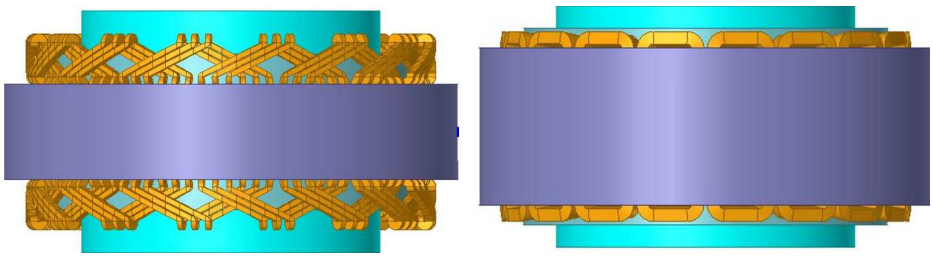

Figure 2.1 – Distributed winding vs concentrated winding [17]

Both concentrated and distributed windings have advantages and disadvantages. For example, concentrated windings (CW) present shorter non-overlapping end turns and higher proportional active length (see Fig. 2.1), this usually means also higher power density and efficiency compared to distributed windings (DW). However, sinusoidal-fed CW produces a rectangular shape magnetic motive force full off harmonic and sub-harmonic content, while DW can provide almost sinusoidal MMF. Considering an induction motor (IM), high harmonic content leads to high rotor bar losses, low efficiency, and eddy torque that overlap the main asynchronous torque [19] [25].
It may be understandable now why tooth-coil winding is used mostly in synchronous machines and distributed winding is the best option for induction motors. IMs with concentrated winding have been previously designed and tested, and results proved that distributed winding is

superior in terms of torque production and rotor bar losses for induction machine applications [20].
Consequently, for the following design, distributed winding, with $q \geqslant 1$, will be chosen.

It is well known that, in a DW, the voltages induced to the same phase coils have a non-zero shift, so the total induced voltage is reduced by the distribution factor

$$k_{d\nu} = \frac{sin(q\frac{\alpha_s \nu}{2})}{q\, sin(\frac{\alpha_s \nu}{2})} \tag{2.2}$$

where $\alpha_s = \frac{2\pi}{Q} p$ is the electric angle between stator slots and ν is the order of the harmonic considered. Furthermore, a two-layer DW could be short pitched by a integer number of slots y_r to reduce harmonics without significantly affecting the first one, this change is taken into consideration by the pitch factor

$$k_{p\nu} = cos\left(\frac{\beta^e \nu}{2}\right) \tag{2.3}$$

where β^e is the electric angle of the short pitching. Finally, the winding coefficient is obtained as:

$$k_{w\nu} = k_{d\nu}\, k_{p\nu}. \tag{2.4}$$

Feeding a DW with symmetrical alternate currents of amplitude I_m produces the famous step curve of rotating magnetomotive force U along the air gap of the machine. For example, it can be demonstrated [2] that a three-phase DW produces a rotating MMF whose fundamental harmonic is equal to:

$$U_1(\alpha,t) = \frac{3}{2}\frac{nqI_m}{\pi} k_w\, cos(\omega t - \alpha) \tag{2.5}$$

where n is the number of conductors per slot.
Generalizing for a m-phase winding and for ν-th order harmonic, the magnitude of the MMF produced by an integer-slot winding can be written as:

$$U_{m\nu} = \begin{cases} U_{m1}\frac{1}{\nu} k_{w\nu}, & \nu = 2km \mp 1, \text{ with } k = 0,1,2... \\ 0, & \nu \in \mathbb{N} \setminus 2km \mp 1 \end{cases} \tag{2.6}$$

where U_{m1} is the amplitude of the fundamental harmonic, for a m-phase winding, according to [14] and [16]. For example, a normal integer-slot three-phase DW produces harmonics of order ν = 1,5,7,11,13... which engrave on rotor losses and torque ripple. Respectively 7^{th},13^{th},... harmonic are synchronous with the fundamental one, while 5^{th},11^{th},... harmonic fields have the opposite direction of rotation.
It is very apparent that the higher the number of phases, the lower the harmonic content generated, since the first non-zero harmonic order, besides the fundamental, would be proportionally higher.

2.2 Multi-phase systems

Three phase motors are certainly the most common and diffused electric motors typology. However, increasing numbers of induction motors are not connected directly to three-phase

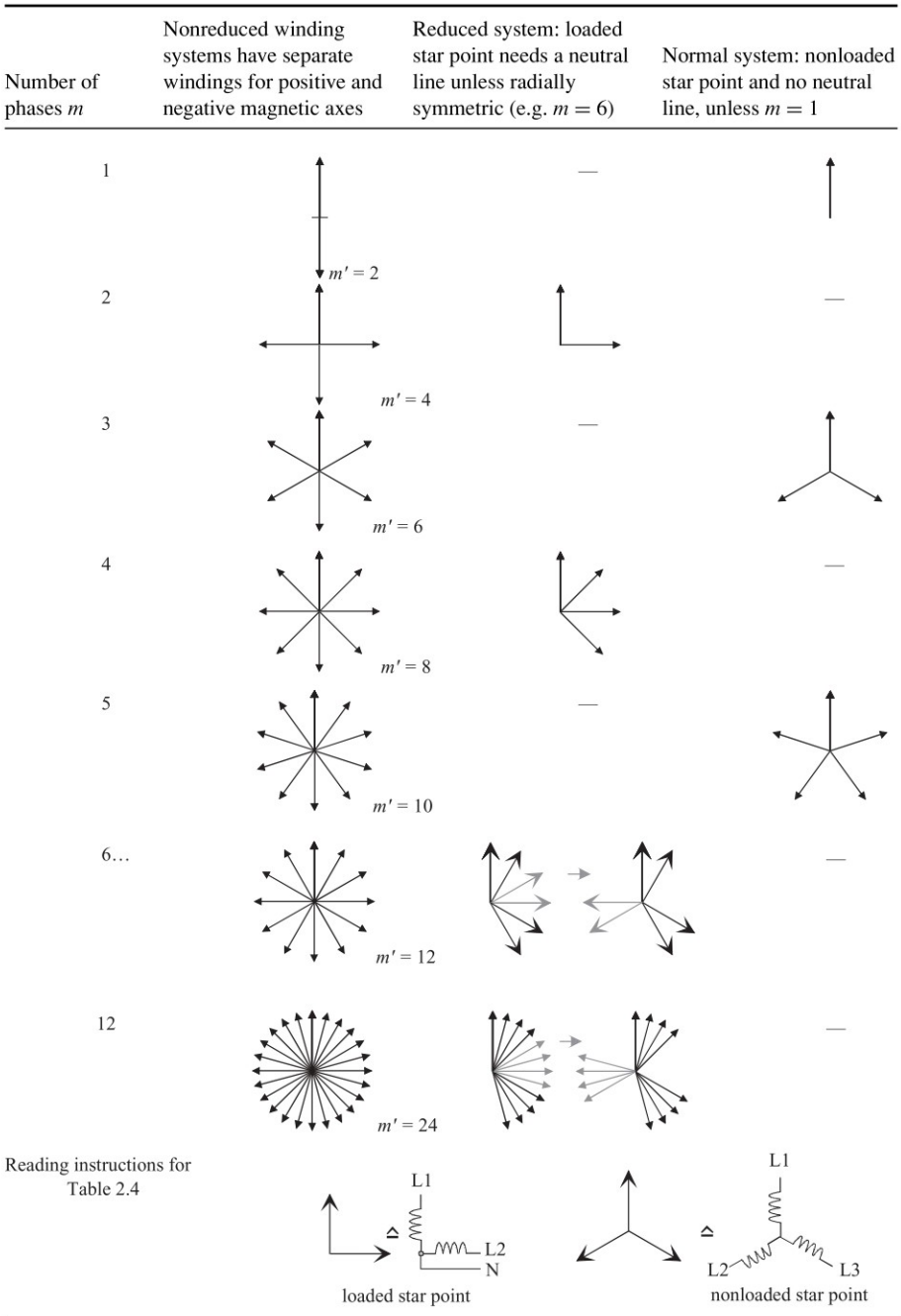

Figure 2.2 – Normal and reduced phase-systems of electrical machines [19]

supplies but to a power electronic converter. The input of which can be connected to a three-phase supply, but the output stage of the converter and the motor winding must have the same number of phases. This requirement can be easily met, so any number of phases may be adopted. The current intense electrification of mobility and means of transport requires higher standards for reliability and fault-tolerant electric machines. Considering a number of phases higher than 3 can certainly provide redundancy and higher system reliability [12].

If multiple phases are present, only one axis of a single-phase winding can be located on a single magnetic axis of the electrical machine. Otherwise, no genuine multi-phase system comes to light. Every system with an even number of phases m can be reduced to a system with half the original number of phases, the so-called reduced system. On the other hand, if m is odd, we have a normal system [19]. Examples of different multi-phase systems are provided in Fig. 2.2.

Reduced systems might imply a loaded star point unless a radially symmetric system can be built again by turning the direction of the suitable phasors by 180 electrical degrees in the system (see the 6-phase example). The loaded star point requires a neutral conductor of its own. With a normal system a nonloaded star point is created, so no neutral line is needed.

For a normal m-phase system the phase angle can be computed as:

$$\alpha_{ph} = \frac{2\pi}{m} \tag{2.7}$$

while for a reduced system we have

$$\alpha_{ph} = \frac{\pi}{m}. \tag{2.8}$$

The number of phases of this machine is set to be $m = 9$ to match reliability levels for safety-critical systems and also guarantee acceptable performance and torque ripple even after one or two phases failures [12]. Correspondingly, the phase angle for this normal system is $\alpha_{ph} = 40°$

Three different types of connection are presented for a 9-phase drive train, as shown in Fig. 2.3:

a. 3x3-phase, composed by 3 different star connections and 3 different power converters

b. 1x9-phase, composed by 1 star connection and 1 power converter

c. 9 galvanically isolated phases each with its own power converter

As stated in [12], the best layout for the application requirement is type c). Having 9 independent phases not only prevents phase-to-phase short-circuit but also allows a more effective thermal separation and cooling. The type of connection will be irrelevant to the design process carried out in the following pages, so it will no longer be discussed.

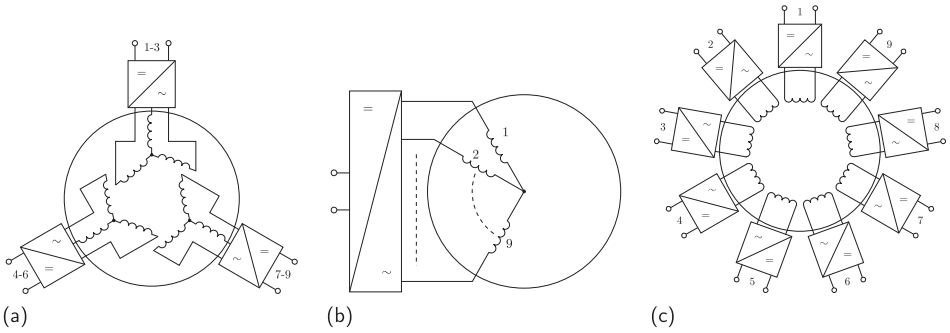

Figure 2.3 – Three different 9-phase connections. a) 3x3-phase system b) 1x9-phase system c) 9 galvanically insulated phases system [12].

2.3 Number of poles and slots

The final choice of pole and slot number will be explained in this section.
Since the supply frequency of the machine is not given, any pole number could be suitable, as far as it is even. Considering the rated power of the machine (see next chapter), only pole numbers between 2 and 8 will be considered.
Speaking of the slot number, a symmetrical two-layer winding is the target we want to achieve to ensure the most sinusoidal MMF possible.

First of all, the machine periodicity number can be defined as the greatest common divisor (GCD) of Q and p:

$$t = GCD\{Q,p\} \tag{2.9}$$

which represents how many electrically equal slots are present in the armature. Furthermore, the electrical angle between two consecutive slots α_s^e has to be taken into consideration:

$$\alpha_s^e = \frac{2\pi}{Q}p \tag{2.10}$$

According to [19], a winding is said to be symmetrical if, when fed from a symmetrical supply, it creates a rotating magnetic field, and the two following conditions must be accomplished:

$$\frac{Q}{m} = 2pq \in \mathbb{N}, \tag{2.11}$$

and for normal systems:

$$\frac{\alpha_{ph}}{\alpha_s^e} = \frac{Q}{mt} \in \mathbb{N}. \tag{2.12}$$

Consider, for example, an integer slot winding. In this case, p and q are always integers so the first condition is already fulfilled. Additionally, the greatest common divider of Q and p is always $t = p$. So the second condition can be simplified in:

$$\frac{Q}{mt} = 2q \in \mathbb{N}. \tag{2.13}$$

This condition of winding symmetry allows only certain values of stator's slots, Q must be a multiple of m. In our case, being $m = 9$, the admitted numbers of slots are Q = 9,18,27,36....

Q	$2p$	t	q
18	2	1	1
27	2	1	1.5
36	2	1	2
36	4	2	1
45	2	1	2.5
45	4	1	1.25
54	2	1	3
54	4	2	1.5
54	6	3	1

Table 2.1 – All possible combinations of $Q = 9,18,27...,54$ and $p = 2,4,6,8$ that allow distributed winding

In order to obtain a near sinusoidal distribution of the MMF in the air gap, a distributed winding is chosen, so it must be $q \geqslant 1$, as stated in Sec. 2.1. Therefore, all possible combinations of poles and slots, that allow a DW, are reported in Tab. 2.1.

Other parameters need to be taken into consideration to choose one combination or another, they are listed below:

- slot pitch, p_s, defined as:

$$p_s = \frac{\pi D}{Q}. \tag{2.14}$$

  This value represents how much space is occupied by a single slot. The smaller the slot pitch, the more difficult to avoid iron saturation in teeth. High slot numbers, given a fixed air gap diameter D, imply significantly small slots and teeth that are not only difficult to realize but also can be easily saturated.
  According to [5] and [19], thanks to the experience from already built machines, a common slot pitch range can be found for asynchronous machines: $10mm \leqslant p_s \leqslant 40mm$. Also, smaller slot pitch values would lead to difficulties during the manufacturing process. Considering the first design air gap diameter, evaluated as described in the following chapter, the slot pitch for every slot number can be calculated. Slot/pole combinations with resulting short pitch out of this range, or near its edges, will be discarded.

- first harmonic winding factor.
  We try to keep k_w as close to 1 as possible. The higher the first harmonic winding factor the higher the induced EMF first harmonic and the torque output are.

- MMF total harmonic distortion (THD).
  To obtain an MMF distribution as close to a sinusoidal wave as possible, the harmonic content of each slot/pole combination can be analyzed using 2.6. As a matter of fact, minimizing the THD will lead to improve efficiency and reduce torque ripple and noise of the machine, as already stated. Defined:

$$THD_U = \frac{\sqrt{\sum_{\nu=2}^{\infty} U_\nu^2}}{U_1}, \tag{2.15}$$

  in the following calculations the THD is evaluated considering the first 100 harmonics.

Q	$2p$	t	q	y_q	k_w	THD [%]	p_s [mm]
18	2	1	1	8	0.9848	9.54	24.4
27	2	1	1.5	12	0.982	5.83	16.3
36	**2**	**1**	**2**	**17**	**0.9924**	**4.40**	**12.2**
36	4	2	1	8	0.9848	9.54	14.0
45	2	1	2.5	21	0.9903	7.55	9.8
45	4	1	1.25	10	0.9830	4.65	11.2
54	2	1	3	26	0.9938	2.64	8.1
54	4	2	1.5	12	0.9820	5.83	9.3
54	6	3	1	8	0.9848	9.54	10.5

Table 2.2 – Distributed winding slot/pole combinations and most valuable parameters

Also, the best short pitch slot number y_p is chosen to minimize the harmonic content in every case ($\beta^e = y_p\ \alpha_s^e$, see 2.3). So the coil span, expressed in number of slots, is given by:

$$y_q = \frac{Q}{2p} - y_p. \tag{2.16}$$

All these important parameters are calculated for each valid DW combination and reported in Tab. 2.2.

One specific combination of slots and poles is shown to fulfill the slot pitch condition and presents a higher first harmonic winding coefficient and lower harmonic content than the other possibilities. So this will be our final choice for the machine design:

$$Q = 36 \quad 2p = 2 \quad q = 2$$

2.3.1 Star of slot and winding scheme

Once the poles and slots are defined, the winding scheme can be drawn.
Again, it can be noticed that the number of phasors of the positive (or the negative) part of each phase is equal to $q = 2$. First, a useful diagram is introduced for better understanding and designing the winding layout: the star of slot [5]. This is a vectorial representation of the electro-motive force induced in a conductor laying inside a specific slot of the machine. All the Q induced EMF have the same magnitude but different angles since the slots take place in different positions along the machine's stator. Every slot is represented by a single phasor, numbered in the same way.
The star of slot is composed of $\frac{Q}{t}$ spokes, each spokes containing t phasors. Indeed, if $t > 1$, at least two electrically identical slots are present, as mentioned before in Sec. 2.1, so they are placed along the same spoke. Consequently, the angle between two consecutive spokes is:

$$\alpha_{spokes} = \frac{2\pi}{Q} t. \tag{2.17}$$

In our case, $t = 1$, so we have 36 spokes and 36 phasors in the diagram, one displaced from the other by $\alpha_{spokes} = 10°$.
Furthermore, the electrical angle occupied by a single phase is $\alpha_{ph} = 40°$, already mentioned in Sec. 2.2, half with positive currents and half with negative ones on the opposite part of

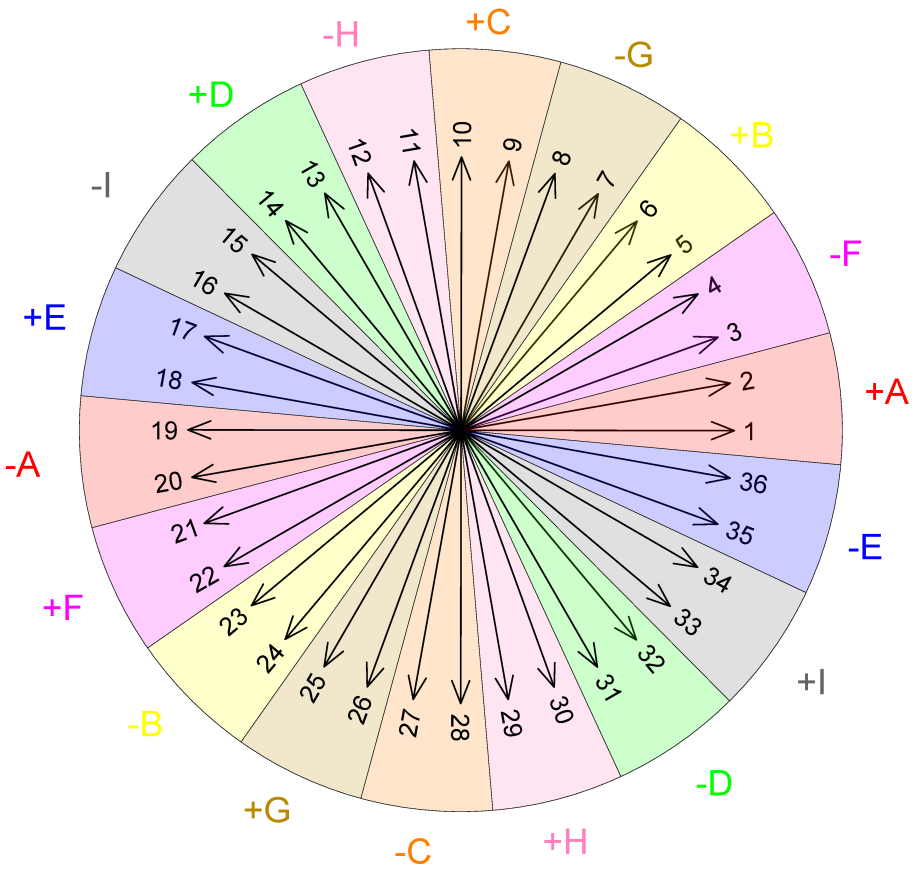

Figure 2.4 – Star of slot for $Q = 36$, $2p = 2$, $m = 9$

the diagram. Each phase zone is underlined in Fig. 2.4 and marked with a different letter and sign.

The star of slot shows how the first layer of the winding has to be done. The second layer can be built with the same disposition but shifted by y_p slots, if the winding is short-pitched. In Fig. 2.5 the complete winding scheme is presented, specifying the conductors' phase in each slot. Phases are marked with letters and respective current directions, with a *plus* if the current enters the drawing plane and a *minus* if the current exits the drawing plane.

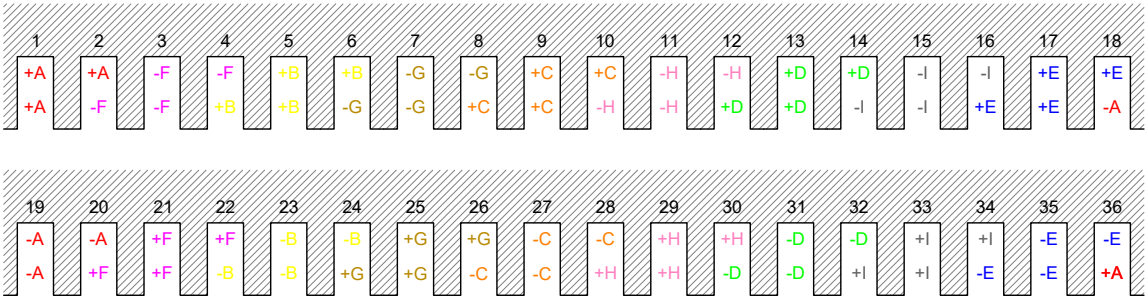

Figure 2.5 – Two-layer distributed winding layout, one slot short pitched

2.3.2 MMF harmonic spectrum

Once the winding is fully designed, the generated magneto-motive force can be computed, as well as its harmonic content. Let's consider a symmetrical 9-phase currents supply:

$$i_a(t) = I_m \sin(\omega t) \tag{2.18}$$

$$i_b(t) = I_m \sin(\omega t + \frac{2\pi}{9}) \tag{2.19}$$

$$i_c(t) = I_m \sin(\omega t + \frac{4\pi}{9}) \tag{2.20}$$

$$i_d(t) = I_m \sin(\omega t + \frac{2\pi}{3}) \tag{2.21}$$

$$i_e(t) = I_m \sin(\omega t + \frac{8\pi}{9}) \tag{2.22}$$

$$i_f(t) = I_m \sin(\omega t + \frac{10\pi}{9}) \tag{2.23}$$

$$i_g(t) = I_m \sin(\omega t + \frac{4\pi}{3}) \tag{2.24}$$

$$i_h(t) = I_m \sin(\omega t + \frac{14\pi}{9}) \tag{2.25}$$

$$i_i(t) = I_m \sin(\omega t + \frac{16\pi}{9}) \tag{2.26}$$

summarized in the column vector $\mathbf{I} = [i_a, i_b, ..., i_i]'$. This currents take place inside the stator slots as described in the winding layout in the previous pages. A slot matrix $\mathbf{K}$ can be defined to mathematically describe the different physical positions of every conductor inside the slots. $\mathbf{K}$ is a m x Q matrix where $\mathbf{K}(i,j)$ is equal to:

- +1, if the j^{th} slot is entirely filled with positive conductors of the i^{th} phase
- +0.5, if the j^{th} slot is half filled with positive conductors of the i^{th} phase
- 0, if no conductors of the i^{th} phase are present in the j^{th} slot
- -0.5, if the j^{th} slot is half filled with negative conductors of the i^{th} phase
- -1, if the j^{th} slot is entirely filled with negative conductors of the i^{th} phase

Some first columns of the matrix are reported in 2.27.

$$\mathbf{K} = \begin{bmatrix} 1 & 0.5 & 0 & 0 & 0 & 0 & 0 & \dots \\ 0 & 0 & 0 & 0.5 & 1 & 0.5 & 0 & \dots \\ 0 & 0 & 0 & 0 & 0 & 0 & 0 & \dots \\ 0 & 0 & 0 & 0 & 0 & 0 & 0 & \dots \\ 0 & 0 & 0 & 0 & 0 & 0 & 0 & \dots \\ 0 & -0.5 & -1 & -0.5 & 0 & 0 & 0 & \dots \\ 0 & 0 & 0 & 0 & 0 & -0.5 & -1 & \dots \\ 0 & 0 & 0 & 0 & 0 & 0 & 0 & \dots \\ 0 & 0 & 0 & 0 & 0 & 0 & 0 & \dots \end{bmatrix} \tag{2.27}$$

Then, the current distribution inside each slot at a given time, can be easily computed:

$$\mathbf{I}_{slot} = \mathbf{K}' \cdot \mathbf{I} \tag{2.28}$$

where $\mathbf{I}_{slot}$ is a Q x 1 column vector containing the current value of each slot at a fixed time. Assuming $I_m = 1\,\text{A}$, the current distribution for this specific winding is reported in 2.6.

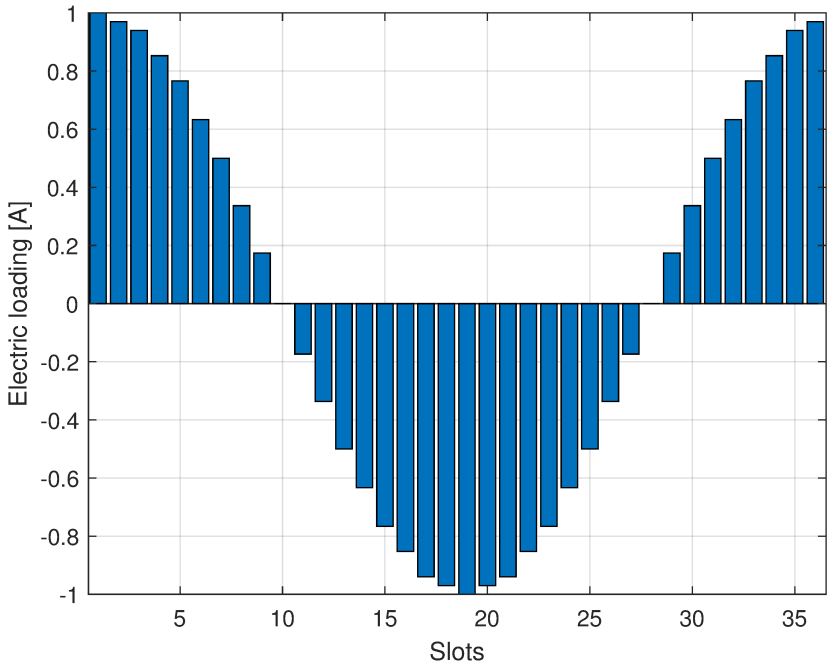

Figure 2.6 – Electric loading over stator slots, considering $I_m = 1\,\text{A}$

The corresponding MMF distribution generated in the air gap can be easily derived thanks to the Ampere-Maxwell law [2]. The result is a step curve (see Fig. 2.7), really close to a sinusoidal shape, as expected. Furthermore, performing a Fourier analysis on the resulting MMF, the harmonic spectrum is evaluated (Fig. 2.8). The non-zero harmonics order is $\nu = 2km \mp 1$, with $k = 0,1,2...$, in accordance with 2.6. The 17^{th} and 19^{th} are particularly low thanks to the short pitch and the overall THD is minimum.

In conclusion, the chosen winding layout allows us to proceed with the induction to the motor design.

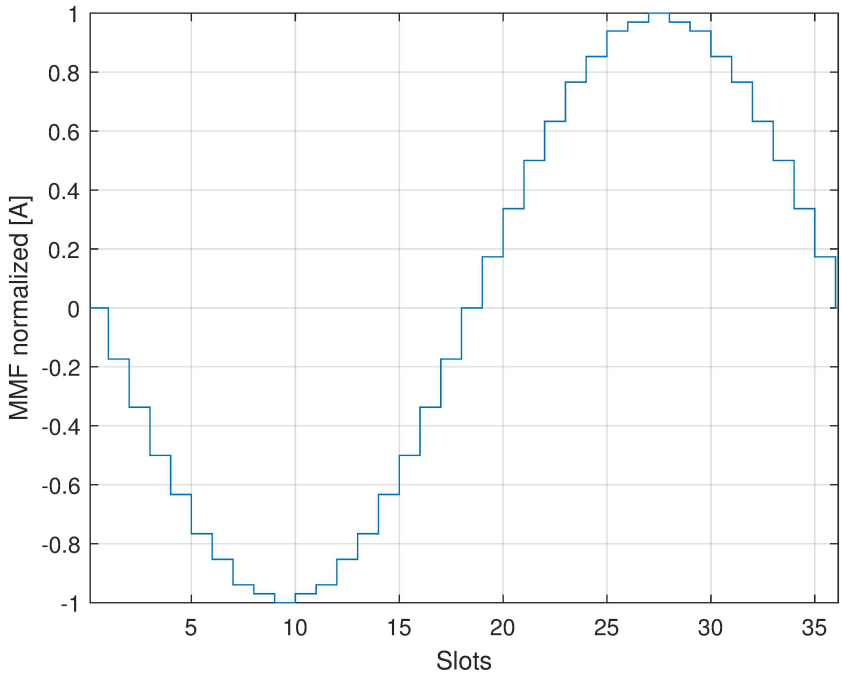

Figure 2.7 – MMF produced by the winding, normalized

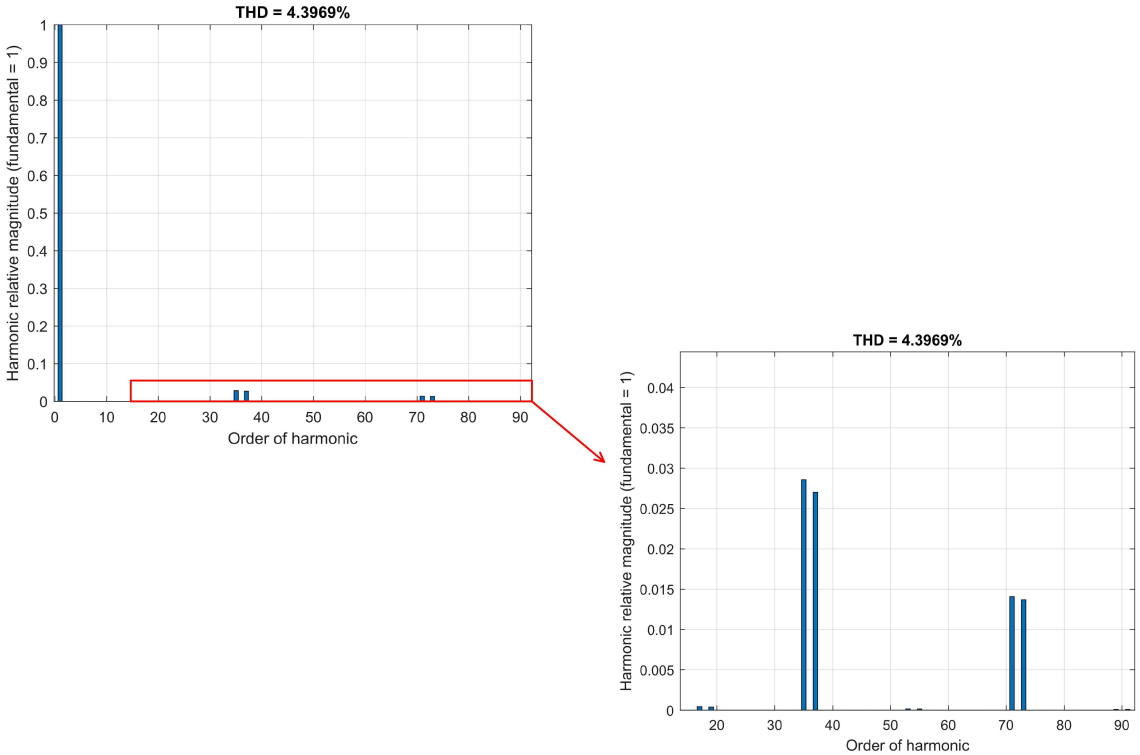

Figure 2.8 – MMF spectrum

3 Machine design

An analytical design process of the induction motor will be presented in this chapter. Starting from Possa's curves approach, the first geometrical values of the machine will be derived. Eventually, the assumption of typical values for current density and magnetic flux density, derived from design experience, will lead to the determination of the complete machine's geometry.

3.1 Main design

This IM's final destination is a test bench at the Technical University of Munich. A multi-phase synchronous motor (SPM) is already been designed and built for the mentioned test bench. This Thesis aims to present an alternative to those with permanent magnets.
The test bench data, which will be the starting point of the design, can be found in [22] and are reported below, in the Tab. 3.1.

Parameter	**Symbol**	**Value**
Input rated power	S	$11\,\mathrm{kVA}$
Rotational speed	n_0	$3000\,\mathrm{min}^{-1}$
Number of phases	m	9
Phase voltage	V_n	$230\,\mathrm{V}$

Table 3.1 – Design specification data [22]

Also, the numbers of poles and slots are already been chosen in 2.3. The supply frequency can be immediately evaluated, knowing its link with the mechanical rotational speed:

$$f = \frac{n_0}{60\ p} = 50\,\mathrm{Hz} \tag{3.1}$$

One of the most significant parameters of the IM is the nominal torque, which will also determine the machine's main dimensions. A first estimation can be derived from the input rated power assuming, as a first hypothesis, the efficiency $\eta = 0.87$ (it is a typical value for this power rating, see also the end of the next chapter), which is typical for IMs with this power rating, and the power factor $\cos\phi = 0.9$.

$$T_n = \frac{S\ \cos\phi\ \eta}{\frac{2\pi\ n_0}{60}} = 27.4\,\mathrm{Nm} \tag{3.2}$$

Several empirical methods may be adopted to determine the dimension starting from the nominal torque and rated power. An example is provided in [22], with Esson's number; In

this case, Possa's curves are adopted. These are an interpolation of already built three-phase IMs in literature and give a generic formulation to estimate the machine's flux Φ, given the maximum torque and the number of pole pairs [5].

$$\Phi = 1.3 \cdot 10^{-3} \frac{T_{max}^{0.55}}{p^{1.1}} = 0.0117\,\text{Wb} \tag{3.3}$$

where $T_{max} = 2\ T_n$.

The magnetic flux is also related to the air gap flux density B_g, the air gap diameter D, and the machine length L.

$$\Phi = \frac{B_g\ D\ L}{p} \tag{3.4}$$

At this point, further assumptions need to be done:

- $B_g = 0.7\,\text{T}$.
  The usual range for IMs is $B_g = \text{from}0.5\,\text{T}\text{to}0.9\,\text{T}$ [5], this value is close to the upper limit when the machine's rated power increases and the pole number decreases. Furthermore, there is no need to stress the machine choosing high magnetic flux density, since the final aim is a prototype for the test bench.
- $\frac{L}{D} = 0.85$.
  The usual range for IMs is $\frac{L}{D} = \frac{\text{from}1.1\text{to}2.3}{\sqrt{2p}}$ [5]. Since no dimensional constraints are imposed, choosing a smaller ratio implies a larger air gap diameter, which allows an easier manufacturing process and usually a better cooling.

Substituting in 3.1, the machine's air gap diameter and the length are given:

$$D = 140\,\text{mm} \quad L = 120\,\text{mm} \tag{3.5}$$

Consequently, $p_s = \frac{\pi D}{Q} = 12.2\,\text{mm}$.

3.2 Stator design

The stator supply current is easily calculated:

$$I_n = \frac{S}{m\ V_n} = 5.31\,\text{A} \tag{3.6}$$

this current will flow through the stator slot conductors. The current density, J_s, in stator winding must not be excessive to guarantee proper thermal dissipation. A common range for values for J_s is mentioned in [19]; $J_s = 5\,\text{A/mm}^2$ is assumed, also according to previous design experience.
The conductors' cross-section S_c can be now evaluated:

$$S_c = \frac{I_n}{J_s} = 1.06\,\text{mm}^2 \tag{3.7}$$

which is achievable with the following commercial wires: $3 \times d_c = 0.5\,\text{mm}^2 + 2 \times d_c = 0.56\,\text{mm}^2$, the real cross-section equal to $S_c = 1.08\,\text{mm}^2$.
The number of series conductors per phase, N_s, can be determined by considering the phase

voltage. Assuming a 5% voltage drop [5], the real voltage on the winding will be $E = 0.95V_n$. Using the bound between winding voltage and generated flux, remembering the winding coefficient described in Chap. 2:

$$N_s \simeq \frac{\sqrt{2}E}{\pi f \ k_w \ \Phi} \simeq 168 \tag{3.8}$$

As a matter of fact, in each stator slot are present

$$n_c = \frac{m \ N_s}{Q} = 42 \tag{3.9}$$

conductors. Since n_c is even, a double-layer winding is possible. No additional parallel paths are allowed because they must be equal to or lower than the number of pole pairs.
Several approximations have been carried out by this point, so a new magnetic flux evaluation is suggested to improve future calculations' precision:

$$\Phi = \frac{\sqrt{2}E}{\pi f \ k_w \ N_s} = 0.0118\,\mathrm{Wb} \tag{3.10}$$

$$B_g = \frac{\Phi \ p}{D \ L} = 0.702\,\mathrm{T} \tag{3.11}$$

The total space occupied by winding copper in each stator slot must be known to define slots geometrical parameters. Moreover, assuming a standard coefficient for the conductors' space filling $k_{fill} = 0.4$, slots' cross-section is given:

$$S_{slot} = \frac{n_c \ S_c}{k_{fill}} = 113.6\,\mathrm{mm}^2 \tag{3.12}$$

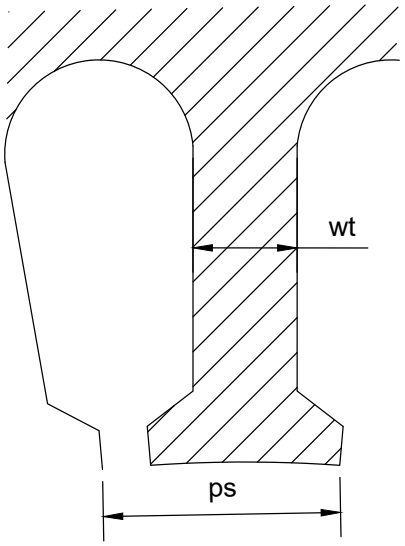

Figure 3.1 – Stator tooth

The next step is the design of the stator tooth, in which the magnetic flux density must be limited ($B_t = 1.7\,\mathrm{T}$) to prevent heavy iron saturation. Gauss law states that the magnetic

flux is preserved, so the flux within the tooth must be equal to the one in the air gap under it. Looking at Fig. 3.1, the following equation can be written:

$$B_t \; w_t \; L_{Fe} = B_g \; p_s \; L \tag{3.13}$$

where $L_{Fe} = k_{pack} \cdot L$ is the real iron length, $k_{pack} = 0.95$ as a standard packing factor for steel sheets is considered. Then, the minimum tooth width is given.

The final stator slot geometry is obtained thanks to a MATLAB code, keeping tooth width and slot's cross-section as close as possible to values previously determined. The results are reported in Fig. A.1 and Tab 3.2.

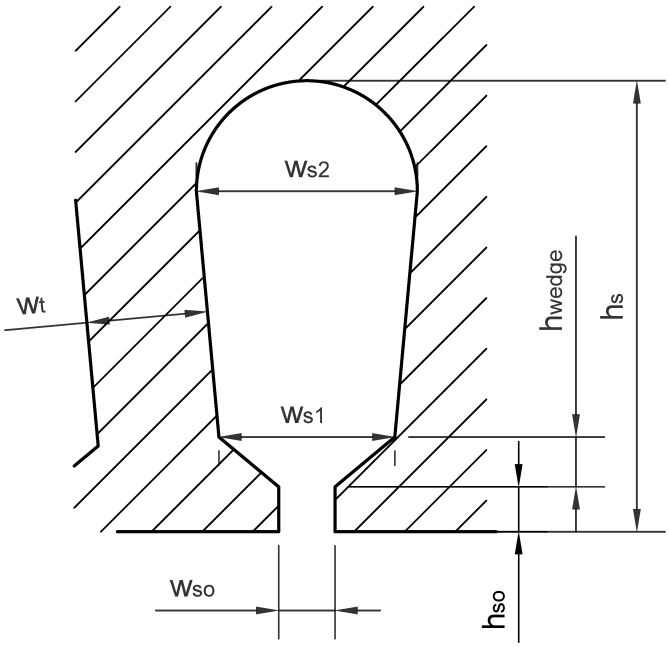

Figure 3.2 – Stator slot

Parameter	Value
w_{so}	2.5 mm
h_{so}	2 mm
h_{wedge}	1.6 mm
w_{s1}	7.5 mm
w_{s2}	9.7 mm
w_t	5.3 mm
h_s	21 mm
S_{slot}	111.2 mm^2

Table 3.2 – Stator slot geometrical parameters

Gauss law is also applied to determine the back iron height (Fig. 3.3), where the maximum magnetic flux will be half of the value calculated in 3.1. Imposing a reasonable value of magnetic flux density in the back iron, $B_{bi} = 1.5\,\mathrm{T}$, we can determine:

$$h_{bi} = \frac{\Phi/2}{B_{bi}\ L_{Fe}} = 34\,\mathrm{mm} \tag{3.14}$$

In this IM the back iron dimensions are significant, which is usual for electrical machines with a low number of pole pairs.

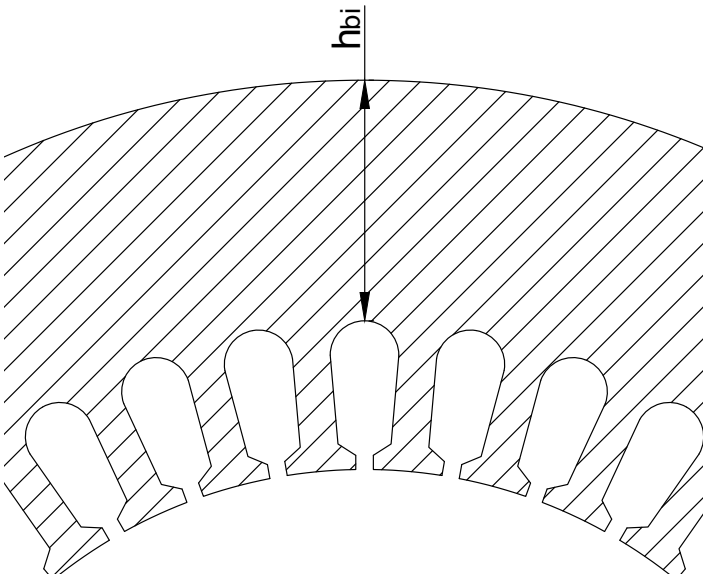

Figure 3.3 – Back iron

Finally, the stator outer diameter is calculated:

$$D_e = D + 2h_s + 2h_{bi} = 250\,\mathrm{mm} \tag{3.15}$$

3.3 Rotor design

Generally speaking, three types of rotors are commonly adopted for asynchronous machines: single cage, double cage, and wound rotor. For power ratings under 50 kW, the first typology is preferred [5]. Moreover, the IM will be connected to an inverter, so no high starting torque is required, which will be guaranteed by the second option and the third one (with additional resistances).

The choice of the air gap length is a trade-off between mechanical and electrical properties. From an electrical point of view, the smaller the air gap, the lower the current needed to magnetize the machine, but tenths of a millimeter gap between the stator and rotor could lead to mechanical issues. Usually, air gaps between 0.5 mm and 2 mm can be found in literature

[19] [5], with higher values for bigger-sized machines. Also, the following empirical formulas are useful guides for a proper choice, reported in [5] and [19]:

$$g = 1\,\text{mm} \cdot \sqrt[4]{\frac{P_n(\text{kW})}{100}} \simeq 0.6\,\text{mm} \tag{3.16}$$

$$g = \frac{0.2 + 0.01 \cdot P_n^{0.4}}{1000} \simeq 0.6\,\text{mm} \tag{3.17}$$

resulting the rotor outer diameter $D_r = D - 2g = 138.8\,\text{mm}$.

The selection of the number of rotor slots, Q_r, plays an important role in avoiding air gap MMF harmonics, which are caused by the interaction between stator slots and rotors'. Some practical rules, as well as already-built slots combinations, are presented in [5]:

- $Q_r \neq Q$
- $|Q_r - Q| \neq 2p$
- Q_r is even and prime number multiple
- Q_r should differ from Q by $25\% - 35\%$

More detailed analyses on MMF harmonics caused by different stator and rotor slot combinations are performed in [11]. As the authors conclude, machines with one pair of poles do not develop any dangerous harmonics. Therefore, it can be expected that such machines are quiet in operation, noise-free, and without high vibrations [6]. Consequently, the selected number of rotor slots is $Q_r = 46$.
A rotor slot skewing equal to α_s^e is also performed to reduce undesired cogging torque. A reduction coefficient is introduced:

$$k_{skew} = \frac{\sin\frac{\alpha_s^e}{2}}{\frac{\alpha_s^e}{2}} \tag{3.18}$$

The rotor bars' shape and material heavily affect the machine's performance. For example, high resistance bars lead to a high starting torque but low efficiency. Furthermore, several bar shapes and their effect on the motor's efficiency and torque characteristics have been studied [21]. In our case, rotor bars will have an inverted trapezoidal round bottom shape and be made of Aluminium.

The induced current in each rotor slot is:

$$I_{bar} = \frac{m\ k_w\ N_s}{Q_r\ k_{skew}}\ I_{sr} = 156.2\,\text{A} \tag{3.19}$$

where $I_{sr} \simeq I\cos(\phi)$ is the active part of I, i.e. the current portion which is actually transmitted to the rotor. Imposing a reasonable value of bar current density $J_{bar} = 3\,\text{A/mm}^2$, the bar's cross-section is given:

$$S_{bar} = \frac{I_{bar}}{J_{bar}} = 52.1\,\text{mm}^2 \tag{3.20}$$

Moreover, the tooth width is evaluated with the same logic used in 3.2:

$$w_{tr} = \frac{B_g\ p_{sr}\ L}{B_{tr}\ L_{Fe}} \tag{3.21}$$

where the magnetic flux density in the rotor tooth is set $B_{tr} = 1.7\,\mathrm{T}$. The whole rotor bars' geometrical parameters (Fig. 3.4 and Tab.3.3) are calculated with the same procedure used in stator slot design.

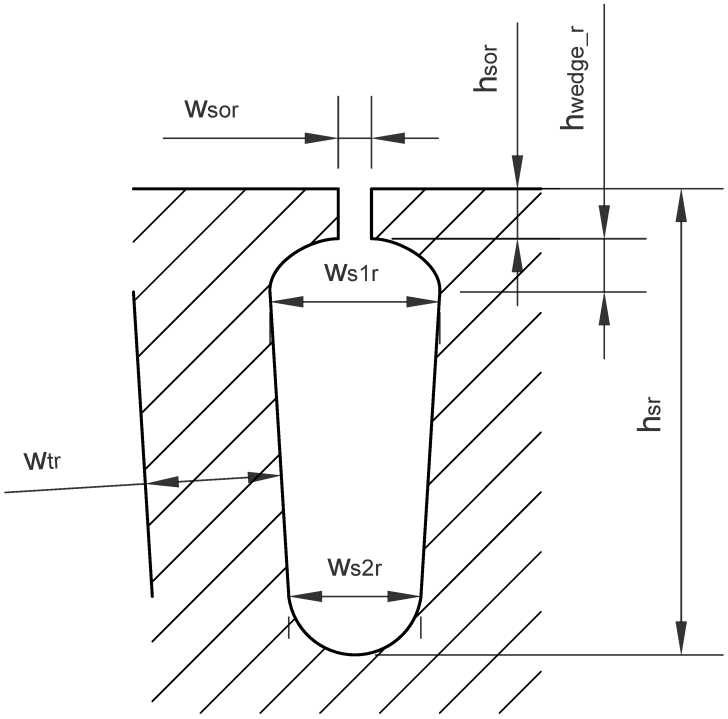

Figure 3.4 – Rotor slot

Parameter	Value
w_{sor}	1 mm
h_{sor}	1.5 mm
h_{wedge_r}	1.2 mm
w_{s1r}	5 mm
w_{s2r}	3.3 mm
w_t	4.1 mm
h_{sr}	17 mm
S_{bar}	53.5 mm^2

Table 3.3 – Rotor slot geometrical parameters

Another step is sizing the two external short-circuit rings. The ring current can be derived from the bar current:

$$I_{ring} = \frac{I_{bar}\ Q_r}{2\pi\ p} = 1143.6\,\mathrm{A} \tag{3.22}$$

A cross-section of 17 mm x 15 mm is chosen to guarantee a ring current density equal to $J_{ring} = 4.5\,\mathrm{A/mm}^2$. This value is higher than the bars' current density because short-circuit

rings have much better cooling, having a bigger heat exchange surface. The rings' diameter, measured in the middle, point will be:

$$D_{ring} = D_r - h_r = 121.8\,\text{mm} \tag{3.23}$$

Finally, the rotor yoke's height is evaluated as already done for the back iron in 3.2. The imposed value of magnetic flux density here is lower, i.e. $B_y = 1.4\,\text{T}$, because here minimizing losses and magnetizing current is possible without heavily affecting the machine's dimensions and weight.

$$h_y = \frac{\Phi/2}{B_y\ L_{Fe}} \simeq 35.9\,\text{mm} \tag{3.24}$$

$$D_y = D_r - 2h_{sr} - 2h_y = 33\,\text{mm} \tag{3.25}$$

At this point, only some mechanical checks on the rotor and the shaft need to be performed.

3.3.1 Mechanical checks

Rotor's static mechanical checks are performed in this subsection. It is relevant to point out that these do not constitute a complete mechanical analysis, but only some preliminary calculations.

First, we want to verify if the rotor can handle the mechanical stress caused by centrifugal force at the maximum speed. Considering the rotor as a smooth steel cylinder, the highest stress σ_{mec} in the rotor is proportional to the square of the angular speed [19]:

$$\sigma_{mec} = C'\ \gamma\ (\frac{D_r}{2})^2\ \omega^2 \tag{3.26}$$

where $C' = 0.823$ is a given constant for steel cylinder, $\gamma = 7800\,\text{kg/m}^3$ is the density of steel, and $\sigma_{max} = 325\,\text{MPa}$ for the considered steel sheets (ISOVAC 350-50A [24]). Then, the maximum rotational speed is given:

$$n_{max} = \sqrt{\frac{\sigma_{max}}{C'\ \gamma\ (\frac{D_r}{2})^2}}\ \frac{30}{\pi} \simeq 30\,000\,\text{min}^{-1} \tag{3.27}$$

which is significantly higher than n_0.

Considering a shaft with a diameter equal to D_y and $1.5L$ long, the bending moment M_b on it is generated by the rotor total weight G_r.

$$M_b = \frac{G_r\ L_{shaft}}{4} \tag{3.28}$$

producing a tensile stress

$$\sigma_t = \frac{32 M_b}{\pi\ D_y^3} \tag{3.29}$$

Obviously, also a shear stress τ is present on the shaft due to the electromagnetic torque produced by the motor. Considering an estimated maximum torque $T_{max} \simeq 60\,\text{N m}$ (as in 3.1):

$$\tau = \frac{16 T_{max}}{\pi\ D_y^3} \tag{3.30}$$

In the end, the equivalent stress can be calculated:

$$\sigma_{eq} = \sqrt{\sigma^2 + 3\tau^2} = 15\,\text{MPa} \tag{3.31}$$

when the maximum stress stated in the datasheet [24] is $\sigma_{max} = 325\,\text{MPa}$, resulting in a safety factor $s.f. = 22$.
These checks will have to be repeated after a detailed analysis of the motor, which will be performed on the following pages.

The final motor's geometry is presented in Fig. 3.5.

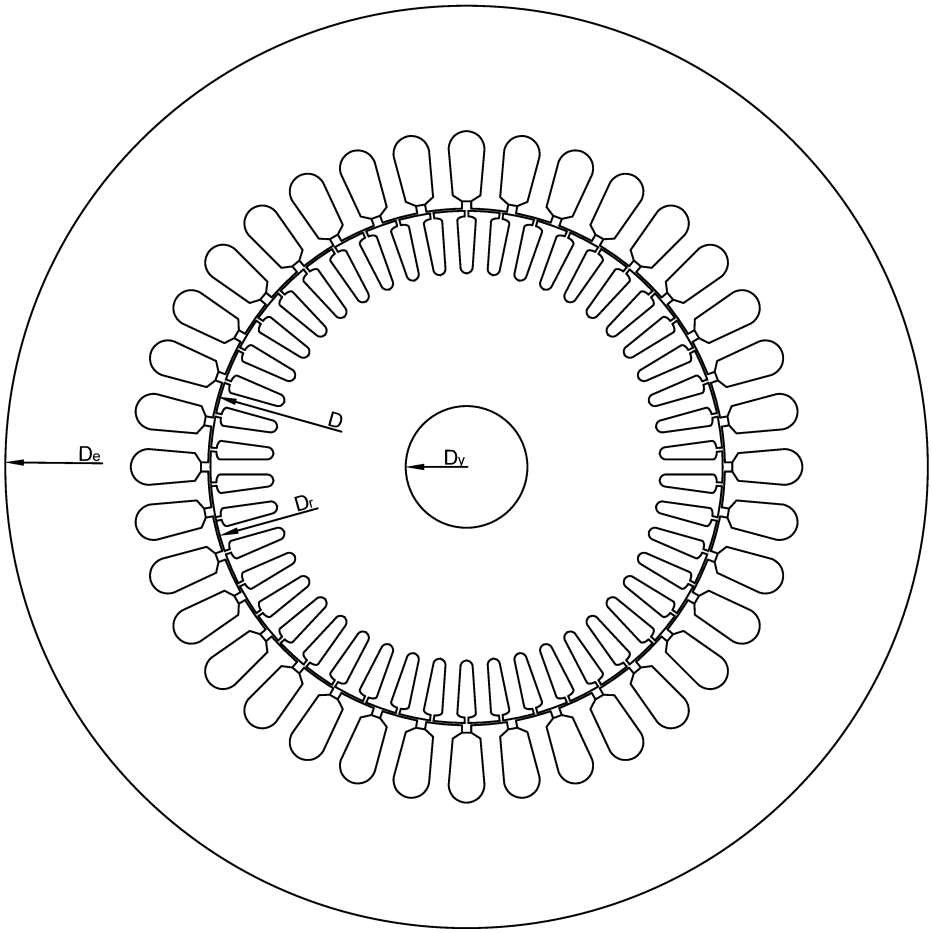

Figure 3.5 – Motor final geometry

4 Analytical analysis

The machine just designed in the previous chapter is now analyzed through analytical methods presented in [5]. This chapter aims to derive the IM's main characteristics and performance. Then, the results will be compared to the requested specifications and design assumptions described in Chap. 3.

4.1 Magnetic circuit

We are now going to consider the magnetic circuit inside the motor, which is dived into five parts: air gap, stator tooth, rotor tooth, back iron, and rotor yoke. Each part's magnetic flux density and magnetic voltage drop are calculated to determine the corresponding magnetizing current (Ampere-turns).

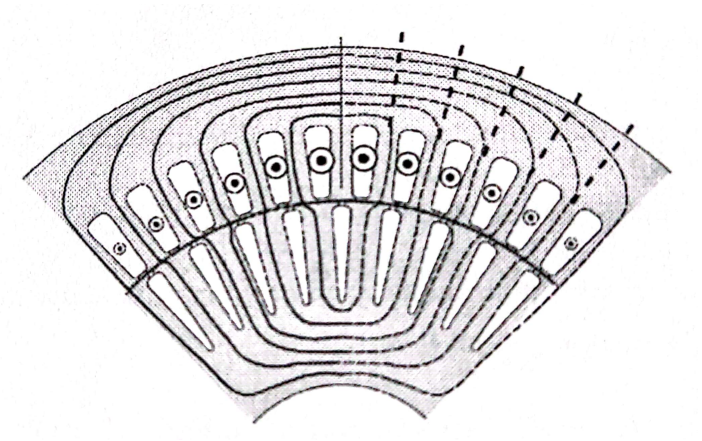

Figure 4.1 – Magnetic circuit of the induction motor [5]

1. **Air gap**
   The magnetic field is not always uniform along the air gap, due to the stator and rotor slot openings. Carter's coefficient is introduced to take into consideration also these irregularities:

$$k_{Carter} = \frac{p_s}{p_s + g - \frac{3}{4} w_{so}} \tag{4.1}$$

   An equivalent smooth air gap can then be defined as the original air gap, incremented by Carter's coefficient of stator and rotor:

$$g' = g \ (k_{Carter_s} \cdot k_{Carter_r}) \tag{4.2}$$

The magnetic field in the air gap H_g is now given, as well as the Ampere-turns needed to magnetize this region:

$$A_g = H_g \; g' = \frac{B_g}{\mu_0} g' = 380.4\,\mathrm{A} \tag{4.3}$$

The air gap magnetization is the most demanding compared to the remaining parts.

2. **Stator tooth**
The magnetic flux density in the tooth, as explained before, is:

$$B_t = \frac{B_g \; p_s \; L}{w_t \; L_{Fe}} = 1.69\,\mathrm{T} \tag{4.4}$$

The corresponding magnetic field H_t is provided by the material's magnetization curve (see datasheet [24]). Consequently, for the stator tooth:

$$A_t = H_t \; h_s = 126.7\,\mathrm{A} \tag{4.5}$$

where h_s is the tooth's height.

3. **Rotor tooth**
The equation are the same to the ones used for the stator tooth.

$$B_{tr} = \frac{B_g \; p_{sr} \; L}{w_{tr} \; L_{Fe}} = 1.72\,\mathrm{T} \tag{4.6}$$

$$A_{tr} = H_{tr} \; h_{sr} = 117.1\,\mathrm{A} \tag{4.7}$$

4. **Back iron**
The magnetic flux density along the back iron is different from point to point and from time to time. To achieve sufficient precision, it is divided into $q_{pp} = 9$ parts. The flux in each portion is:

$$\Phi_k = \frac{\Phi}{2} \int_0^{\frac{\pi}{2}\frac{k}{q_{pp}}} \cos x \, dx \tag{4.8}$$

and

$$B_k = \frac{\Phi_k}{h_{bi} \; L_{Fe}} \tag{4.9}$$

where the maximum flux density is $B_{bi} = 1.52\,\mathrm{T}$. The magnetic field of each section is calculated and the Ampere-turns are evaluated along the back iron middle line, then summing up:

$$A_{bi} = 75.5\,\mathrm{A} \tag{4.10}$$

5. **Rotor yoke**
The same procedure of the back iron is followed here, resulting:

$$B_y = 1.4\,\mathrm{T} \tag{4.11}$$

$$A_y = 16.8\,\mathrm{A} \tag{4.12}$$

The yoke's magnetization cost is the lowest because the magnetic path is relatively short and the flux density is modest. In some cases it can also be neglected.

Summing all machine's parts the magnetic circuit is complete. The total Ampere-turns are equal to:

$$\sum H \cdot l = 716.6\,\mathrm{A} \tag{4.13}$$

The saturation coefficient and a new equivalent smooth air gap, which takes into consideration the complete machine magnetization, are calculated:

$$k_{sat} = \frac{\sum H \cdot l}{A_g} = 1.88 \quad g'' = g'\ k_{sat} = 1.3\,\mathrm{mm} \tag{4.14}$$

Considering the chosen winding, the Ampere-turns will be produced by the magnetization current I_μ flowing through the winding conductors:

$$\sum H \cdot l = \frac{m\ k_w\ N_s\ \sqrt{2} I_\mu}{2p\ \pi} \tag{4.15}$$

resulting $I_\mu = 2.12\,\mathrm{A}$.
The ratio between the magnetizing current and the whole nominal current is $\frac{I_\mu}{I_n} = 39.9\%$. On healthy machines this ratio is usually under 40% because we do not want to spend too much current for magnetization and not for active power.
Finally, it is possible to calculate the magnetizing inductance as:

$$L_m = \frac{\hat{\Lambda}}{I_\mu} = \frac{m\ \mu_0}{\pi} \left(\frac{k_w\ N_s}{2p} \right)^2 \frac{D\ L}{g''} = 0.328\,\mathrm{H} \tag{4.16}$$

4.2 Leakage inductances

In this section, the main leakage inductances will be calculated with semi-empirical formulas presented in [5]. The aim is to fully determine the machine's equivalent circuit.

Stator slot leakage inductance
A small part of the flux generated by winding conductors does not cross the air gap and links only with stator slots. The leakage inductance of the stator slot is:

$$L_{\sigma slot} = \mu_0\ q\ 2p\ n_s^2\ L\ k_{slot} = 2\,\mathrm{mH} \tag{4.17}$$

where k_{slot} is a geometrical coefficient depending on slot's shape and geometrical parameters (see A.1). In this case $k_{slot} = 1.92$.

Rotor slot leakage inductance
In rotor slots the same phenomenon is present. Considering the rotor's shape and geometry, $k_{slot_r} = 2.92$. The rotor slot's leakage inductance, referred to the stator:

$$L_{\sigma slot_r} = \frac{m}{Q_r} \left(\frac{k_w\ N}{k_{skew}} \right)^2 \mu_0\, L\, k_{slotr} = 2.4\,\mathrm{mH} \tag{4.18}$$

Skewing leakage inductance
Since a rotor skewing is performed (Sec. 3.3), its leakage inductance is calculated:

$$L_{\sigma skew} = L_m\ (1 - k_{skew}^2) = 0.83\,\mathrm{mH} \tag{4.19}$$

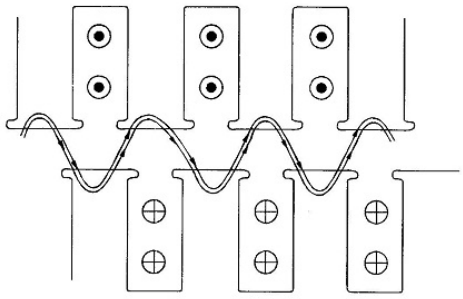

Figure 4.2 – Zig-zag flux leakage [23]

Zig-zag leakage inductance
This type of leakage is caused by the interaction of stator and rotor teeth. The magnetic flux "jumps" from one tooth to the other without linking any conductor, Fig. 4.2.

$$L_{\sigma zz} = \mu_0 \; q \; 2p \; n_s^2 \; k_w^2 \; L \left[\frac{(w_{t1} + w_{t2})^2}{m \; g \; 4(p_s + p_{sr})} \right] = 0.74\,\text{mH} \tag{4.20}$$

where $w_{t1} = p_s - w_{so}$ and $w_{t2} = p_{sr} - w_{sor}$ are the stator and rotor teeth's width close to the air gap.

High-order harmonics leakage inductance
Also called "belt" leakage inductance, it is estimated by means of practical experimental equation:

$$L_{\sigma\nu} = 3.65 \times 10^{-3} k_B \; L_m = 1.2\,\text{mH} \tag{4.21}$$

where k_B is a coefficient depending on number of slots and poles (A.2), in this case it can be considered to be 1.

Leakage inductance on the end winding
It is calculated as:

$$L_{\sigma ew} = \mu_0 \; q^2 \; 2p \; n_s^2 \; L_{ew} \; \lambda_{ew} = 2.2\,\text{mH} \tag{4.22}$$

assuming $\lambda_{ew} = 0.35$ as an empirically given coefficient for imbricated winding and the estimated end winding's length $L_{ew} = 2.5\frac{D}{p}$.

Total
Summing all the previously calculated leakage inductances, the total one is obtained:

$$L_\sigma = L_{\sigma slot} + L_{\sigma slot_r} + L_{\sigma skew} + L_{\sigma zz} + L_{\sigma\nu} + L_{\sigma ew} = 9.4\,\text{mH} \tag{4.23}$$

Referring it to the main inductance L_m, the following ratio is given:

$$\frac{L_\sigma}{L_m} = 2.9\% \tag{4.24}$$

It may be interesting to compare this number to common IMs: this ratio is usually about 10% for three-phase induction motors. Since the total leakage inductance is low, a high value of maximum torque is expected.

4.3 Losses and efficiency

The motor losses and efficiency at the nominal working point are now analytically evaluated. The main loss sources are the current flowing in the winding conductors, the varying magnetic flux inside the stator iron, the induced current in the rotor bars and rings, and mechanical losses. The magnetic flux in the rotor iron does not present a significant relative frequency (as a matter of fact, $f_r = s\,f$), because the rotor rotation is almost synchronous to the magnetic field generated by the stator winding. Consequently, its losses due to eddy current and iron hysteresis are negligible.

4.3.1 Stator losses

First, the total length of a conductor, considering also the end winding, is:

$$L_c = L + L_{ew} = 470\,\text{mm} \tag{4.25}$$

Considering a winding working temperature of 120°, the copper resistivity is $\rho_{Cu} = 2.35 \times 10^{-8}\,\Omega\,\text{m}$. The winding resistance of each phase is given:

$$R_s = \rho_{Cu}\frac{L_c}{S_c}N_s = 1.72\,\Omega \tag{4.26}$$

The total Joule losses of the stator winding are equal to:

$$P_{js} = m\ R_s\ I_n^2 = 436.4\,\text{W} \tag{4.27}$$

Moreover, the iron losses from the teeth and back iron need to be considered. The maximum value of stator tooth flux density is $B_t = 1.69\,\text{T}$ and in the back iron $B_{bi} = 1.52\,\text{T}$. As reported in the specific losses characteristic of the considered steel sheet, at 50 Hz [24]:

- $B_t = 1.69\,\text{T} \longrightarrow\ p_{sp\_t} = 4\,\frac{\text{W}}{\text{kg}}$
- $B_{bi} = 1.52\,\text{T} \longrightarrow\ p_{sp\_bi} = 3.2\,\frac{\text{W}}{\text{kg}}$

The respective weight of teeth and back iron is:

$$G_t = \gamma_{Fe}\ Q\ h_s\ w_t\ L_{Fe} = 3.6\,\text{kg} \tag{4.28}$$

$$G_{bi} = \gamma_{Fe}\ \pi(D_e - h_{bi})\ h_{bi}\ L_{Fe} = 20.5\,\text{kg} \tag{4.29}$$

where $\gamma_{Fe} = 7710\,\text{kg/m}^3$ [24]. Furthermore, sheets' imperfections caused by the manufacturing process are taken into consideration with two coefficients for the teeth ($k_{magg\_t} = 2$) and for the back iron ($k_{magg\_bi} = 1.5$) [5].
The total losses due to eddy currents and hysteresis in the stator iron:

$$P_{Fe} = k_{magg\_t}\ G_t\ p_{sp\_t} + k_{magg\_bi}\ G_{bi}\ p_{sp\_bi} = 125.6\,\text{W} \tag{4.30}$$

4.3.2 Rotor losses

The current value in rotor bars and rings are already known from the design stage (3.3). The Joule losses in the rotor are calculated, as already done for the stator's:

$$P_{jr} = \rho_{Al} \left(Q_r \frac{L}{S_{bar}} I_{bar}^2 + 2 \frac{\pi (D_r - h_{ring})}{S_{ring}} I_{ring}^2 \right) = 256.6\,\mathrm{W} \tag{4.31}$$

where $\rho_{Al} = 4 \times 10^{-8}\,\Omega\,\mathrm{m}$ is the Aluminium resistivity at 120°. The rotor resistance in the equivalent circuit (Sec. 4.4), referred to the stator's point of view, is obtained:

$$R_r = \frac{P_{jr}}{m\ I_{sr}^2} = 1.23\,\Omega \tag{4.32}$$

As already said, the iron losses in the rotor can be neglected since the flux density frequency is almost zero.

The mechanical losses are estimated by the following semi-empirical formula, as a function of the machine's mechanical power and rotational velocity:

$$P_{mec} = (0.6 - 0.8)\ P_n(\mathrm{kW})\ \sqrt{n(\mathrm{rpm})} \simeq 330\,\mathrm{W} \tag{4.33}$$

4.3.3 Efficiency

The total losses and the nominal efficiency can be calculated now. Considering the worst case, a supplementary 10% is added to the losses sum to take into account the contribution of the additional losses that can not be easily estimated analytically [5]:

$$P_{loss} = 1.1(P_{rs} + P_{Fe} + Pjr + P_{mec}) = 1270\,\mathrm{W} \tag{4.34}$$

Then, the nominal efficiency is:

$$\eta = \frac{S\ \cos\phi - P_{loss}}{S\ \cos\phi} = 87.3\% \tag{4.35}$$

which is a typical value also for common three-phase IMs with similar power ratings [5], respecting the design's initial assumptions 3.1.

4.4 Equivalent circuit and performance

The simplified equivalent circuit [2][5] is a powerful circuital representation of the induction motor. The whole motor behavior is reduced to a single-phase circuit,Fig. 4.3, so the main machine's characteristics, such as nominal, maximum, and starting torque, can be derived throughout its solution.

Most of its parameters have already been evaluated before and are reported here:

- $R_s = 1.72\,\Omega$ is the stator winding's resistance
- $X_\sigma = \omega L_\sigma = 2.95\,\Omega$ do to flux leakage

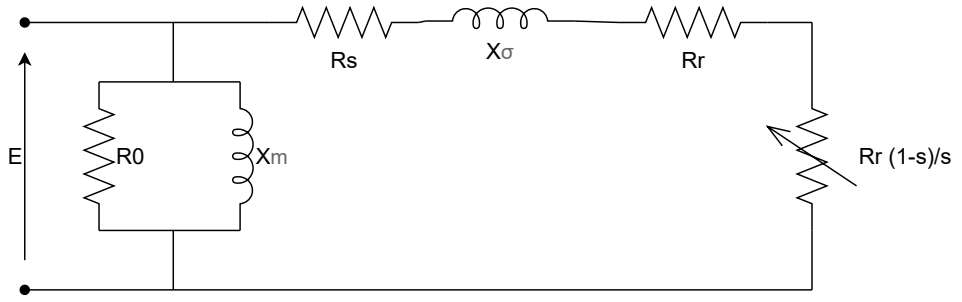

Figure 4.3 – IM's simplified equivalent circuit

- $R_r = 1.23\,\Omega$ is the rotor's equivalent resistance
- $X_m = \omega L_m = 103\,\Omega$ due to machine's magnetization
- $R_0 = \frac{E^2}{P_{Fe}} = 380\,\Omega$ represents the iron losses

Varying the rotor's slip factor, defined as:

$$s = \frac{n_0 - n}{n_0} \tag{4.36}$$

where n is the rotor's actual rotational velocity, the output torque can be computed by solving the circuit and evaluating the dissipated power on the variable resistance, which symbolizes the output mechanical power:

$$T(s) = \frac{m\,p}{\omega} \frac{E^2}{\frac{R_s^2+X_\sigma^2}{R_r} s + 2R_s + \frac{R_r}{s}} \tag{4.37}$$

The nominal slip factor can be computed by a power balance under nominal conditions:

$$s_n = \frac{P_{jr}}{P_n + P_{mec} + P_{jr}} = 2.8\% \tag{4.38}$$

where P_n is the nominal mechanical output power on the shaft, resulting a nominal rotational velocity:

$$n_n = n_0\,(1 - s) = 2917\,\mathrm{min}^{-1} \tag{4.39}$$

Solving the circuit for s_n, the nominal torque is given 4.4:

$$T_n = 28.4\,\mathrm{Nm} \tag{4.40}$$

and a nominal power factor $\cos\phi = 0.907$. These values, as well as estimated efficiency (4.3.3), are very close to the first design hypothesis and specifications in Sec. 3.1, which confirms the design process validity.

Solving the equivalent circuit for different values of slip and rotor velocity, the mechanical characteristic is drawn in Fig. 4.4. The maximum and starting torque are higher than expected, especially if we compare them to a typical three-phase IM. The mechanical checks performed in 3.3.1 are executed one more time, considering the new maximum torque from the analysis, and the results are still acceptable.
This analysis will be compared and verified with FEA results.

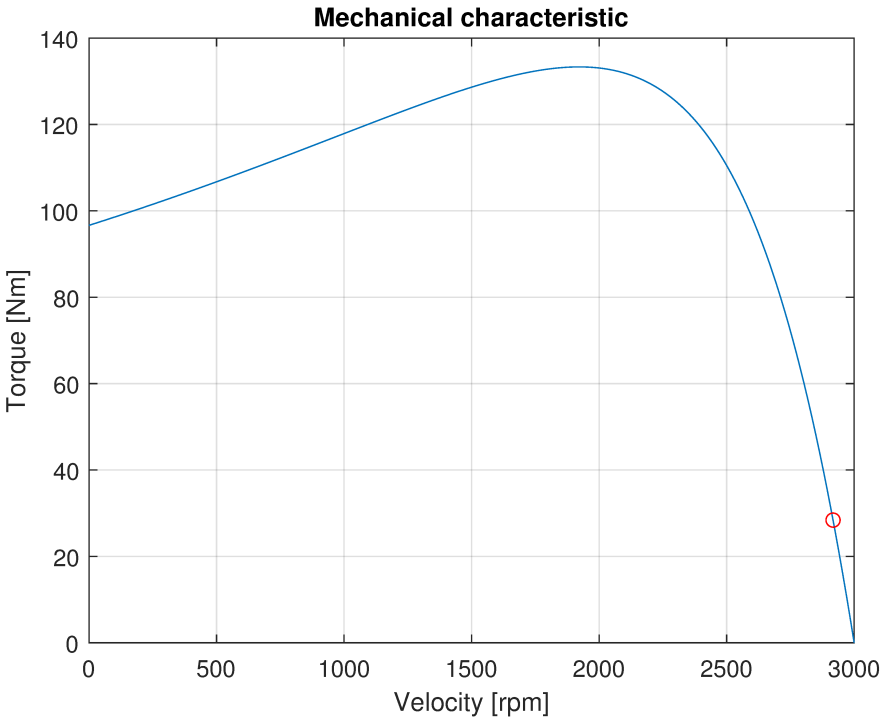

Figure 4.4 – IM's mechanical characteristic, the nominal working point is underlined

5 Genetic algorithm optimization

After the first design of the machine, a genetic algorithm (GA) is created and executed in the MATLAB ambient to improve the motor characteristics such as efficiency, reliability, dimensions, and weight. So in this chapter, a detailed description of the adopted GA for motor optimization is presented, and its results are reported and deeply discussed.

5.1 Genetic algorithms

Genetic algorithms may be addressed as powerful optimization tools used for difficult problems, which can be constrained or unconstrained, based on the natural selection principle. Despite GAs being present since the 1970s, they are still one of the most up-to-date artificial intelligence techniques. Applications of this optimization process can be found in Network routing protocols, image processing, data mining, and computer gaming [15].

Given a random initial population of N individuals in the research space, natural and evolution processes like selection, crossover, and mutation are performed on each individual to produce a new generation. Only the fittest ones will survive, ensuring quality in successive generations will be better. Once a sufficient quality is met the reproduction can be stopped, and the best individual chosen as the optimized output. The main flowchart of a standard genetic algorithm is presented in Fig. 5.1, and a brief explanation of each step will follow [4].

- **Population**
  Every individual is a vector constituted by n design variables $\mathbf{X} = [x_1, x_2, \ldots, x_n]$, each of them bounded between its minimum and maximum values. In this case, a binary GA is adopted, so every x_i variable is expressed in a binary number and, once merged with the other variables, the complete chromosome of a population member is obtained. The initial population is randomly generated, considering the feasible space given by the boundary conditions.
- **Objective and fitness functions**
  The definition of an objective function $O(\mathbf{X})$ is essential in GAs and represents the characteristics that are meant to be optimized by the algorithm. The overall cost or the final performances are common examples [7]. However, this simple function is not always the best way to determine when an individual is better than the other because also physical constraints or competitive features need to be met. So, the fitness function $F(\mathbf{X})$ is introduced. It is defined as a combination of one or more objective functions and penalties $g(\mathbf{X})$ based on the overall results we want to achieve by optimization. The aim will be to maximize (or minimize) this function through the generations to obtain the best possible individual. Further details on the choice of $F(\mathbf{X})$ will be given in the following section.

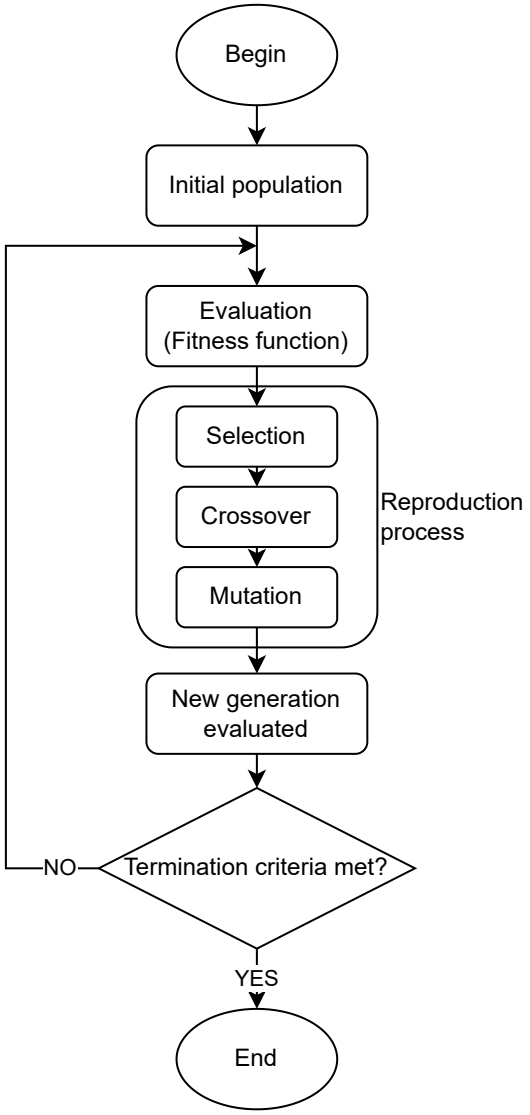

Figure 5.1 – Genetic algorithm technique flowchart [15]

- **Selection**
  In this reproduction step, the old generation members are selected to form the new generation. The selection can be a deterministic sampling: the individuals with the best fitness are preferred and the worst ones are simply discarded.
  However in this work, stochastic sampling is adopted. The selected individuals are chosen according to a probability based on the ratio between their fitness and the average one: $p_i = \frac{F(\mathbf{X}_i)}{F_{avg}}$.

- **Crossover**
  Two selected strings, also called parents, are mated to create two new offspring or children. Every child's gene or chromosome part is randomly chosen between one of the two parents.
  The number of the generated children that join the new generation during every iteration

is expressed by the crossover ratio CR multiplied by N. The higher CR, the more children will come to life.

Parent 1									
1	0	0	0	1	0	1	1	0	1
Parent 2									
1	1	1	0	1	0	1	0	0	0

Child 1									
1	0	1	0	1	0	1	0	0	0
Child 2									
1	1	0	0	1	0	1	1	0	1

Figure 5.2 – Uniform crossover example

- **Mutation**
  A bit of a string of the new population is selected according to the predefined probability p_m and swapped from 0 to 1, or vice versa. The mutation process allows deviations and random changes that help explore the search space for new and unpredictable individuals. On the other hand, it has been noticed in [4] that relatively high mutation probability can lead to instability and make the solution convergence harder to reach because it can alter the selection process of the algorithm.

Before mutation									
1	1	0	1	0	0	1	0	0	1

After mutation									
1	1	0	0	0	0	1	1	0	1

Figure 5.3 – Mutation example

5.2 Motor optimization

In this section, the genetic algorithm procedure is applied to the optimization of the previously designed 9-phase motor. This process aims to find the best combination of design variables to reach the desired IM's features, i.e., maximize the chosen fitness function. After various simulations, the best results will be reported and discussed also considering different algorithm parameters.

The analytical analysis described in Chap. 4 is used to determine the motor performance, given the input geometrical values, during every iteration.
Only a simplified thermal model is added to determine the stator winding relative temperature Θ_w to the external air. The model is a simple lumped thermal network, in which only the

stator copper losses are considered since they are the most relevant stator loss. Their heat flows through two thermal resistances: R_N between the slot copper and the stator iron and R_F, between the iron and the external air, estimated with the following formulas [4].

$$R_N = \left(\frac{w_{ins}}{\lambda_{ins}} + \frac{1}{\alpha_{ins}}\right) \frac{1}{\pi DL\left[\frac{w_s}{p_s} + \left(1 + \frac{2\pi}{Q}\right)\frac{h_s}{p_s}\right]} \tag{5.1}$$

where w_{ins}, λ_{ins}, and α_{ins} are the insulation's width, thermal conductivity, and thermal resistance coefficient. Commercial insulation sheet parameters for motor windings are considered.

$$R_F = \frac{1}{\alpha_{ext}} \frac{1}{r_{ext}\pi DL\left(1 + \frac{2\pi}{Q}\frac{w_s}{p_s} + \frac{\pi B_g}{2p\,B_b{}^i}\right)} \tag{5.2}$$

where α_{ins} is the external air thermal transmission coefficient, and r_{ext} is the ratio between the external frame surface to the outer stack surface, it is taken equal to 3 considering common IM's shells.
Finally, the copper relative temperature is estimated as:

$$\Theta_w = P_{js}(R_N + R_F) \tag{5.3}$$

The winding temperature will be extremely impactful on the motor's reliability and its selection in the GA, as we will discuss in the following pages.

5.2.1 Design variables

Name	Symbol	Minimum	Maximum	Bits N.
Main variables				
Bore diameter	D	120 mm	160 mm	10
Stack length	L	100 mm	140 mm	10
Air gap	g	0.5 mm	0.7 mm	12
Supply current density	J	3 A/mm^2	7 A/mm^2	12
Stator variables				
Back iron height	h_s	27 mm	40 mm	12
Slot height	h_s	15 mm	27 mm	12
Slot wedge height	h_{wedge}	1.2 mm	2.1 mm	12
Slot width	w_{s1}	5 mm	9.5 mm	12
Rotor variables				
Slot height	h_{sr}	13 mm	21 mm	12
Slot wedge height	h_{wedge_r}	0.8 mm	1.7 mm	12
Slot width	w_{s1r}	3 mm	7 mm	12
Yoke diameter	D_y	31 mm	36 mm	10
Ring height	h_{ring}	13 mm	21 mm	8
Ring width	w_{ring}	12 mm	18 mm	8

Table 5.1 – Optimization design variables

Great attention has been dedicated to the choice of design variables and their limits. First of all, not all motor attributes can be modified. This is the case of the number of poles, stator and rotor slots, and supply frequency, as already systematically described in the first chapters.
Every design variable is independent of the others and is presented in Tab. 5.1, as well as its minimum, maximum, and number of bits occupied. It may be worth noticing that the valid range of each variable is set considering small variations (usually around $\pm 20\%$) of the first design geometrical values (see Chap. 3), or the common values suggested from experience. The vector $\mathbf{X}$ contains all x_k motor design variables.

Each input is expressed as a binary variable with a different number of bits. This number is a trade-off between the required precision and the computational cost of the algorithm.

5.2.2 Fitness function selection

Defining a precise fitness function is one of the most challenging and relevant parts of the GA writing process. Since population members will be evaluated and selected when compared to the others thanks to their fitness ranking, an accurate function will not only determine a proper selection but also reach the overall algorithm purpose.
Mathematically speaking, we can define it as [4]:

$$F(\mathbf{X}) = \begin{cases} O(\mathbf{X}) & if\ O(\mathbf{X}) > 0 \\ 0 & otherwise \end{cases} \tag{5.4}$$

This optimization aims, first and foremost, to maximize IM efficiency, keep its weight G under certain limits, and guarantee sufficient reliability standards. As stated in [8], induction motors' reliability and lifetime can be severely affected by external ambient contamination, poor cooling or winding overtemperature, improper insulation system, mechanical vibrations, and stresses. Consequently, concerning the last point, great attention has been dedicated to the stator winding relative temperature Θ_w, as well as the stator slots filling factor and insulation, considering a motor continuous duty (D1).
The objective function is than defined as a weighted linear combination of the listed properties, normalized:

$$\begin{aligned} O(\mathbf{X}) &= O_1(\mathbf{X}) + O_2(\mathbf{X}) + O_3(\mathbf{X}) = \\ &= w_1\ \eta(\mathbf{X}) + w_2\ \frac{G_M - G(\mathbf{X})}{G(\mathbf{X})} + w_3\ \frac{\Theta_M - \Theta_w(\mathbf{X})}{\Theta_w(\mathbf{X})} \end{aligned} \tag{5.5}$$

The target weight is set to $G_M = 50\,\mathrm{kg}$, similar to the weight of the firstly designed motor in the previous chapters; while the target winding relative temperature is chosen $\Theta_M = 80\,^\circ\mathrm{C}$, considering common design experience and typical motors' insulation rating classes 5.4. The function weights w_k are chosen to maximize the efficiency as much as possible, keeping the motor's weight and the winding temperature under their target value.

Usually [4] [7], $F(\mathbf{X})$ is modified adding some penalty terms $g_k(\mathbf{X})$ to meet the initial design specifications or ensure real manufacturing feasibility, resulting:

$$F'(\mathbf{X}) = F(\mathbf{X}) - \sum_k p_k\ g_k(\mathbf{X}) \tag{5.6}$$

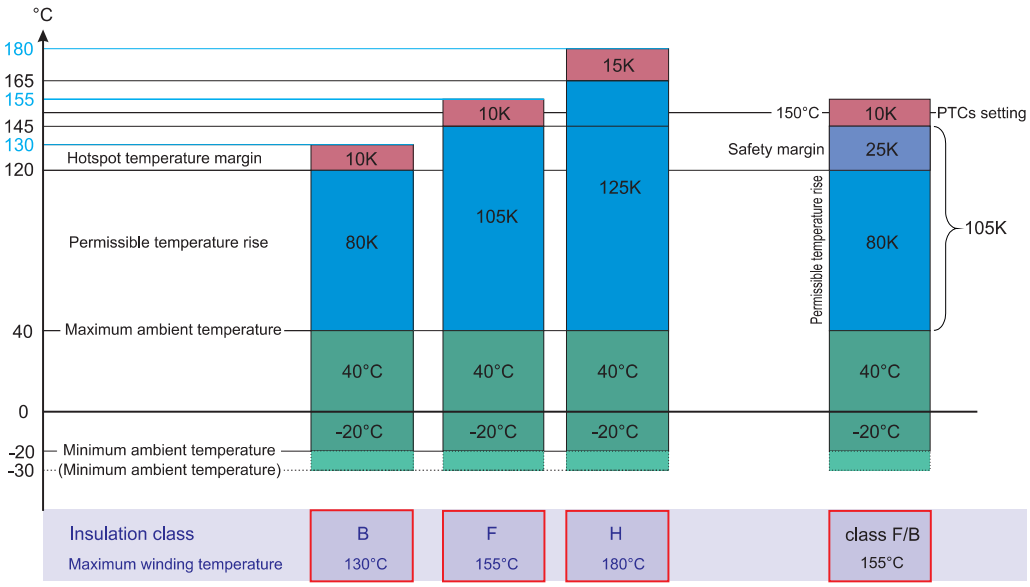

Figure 5.4 – IEC motor winding insulation classes [10]

where the penalty weights p_k are defined as $p_k = 0$ if $g_k(\mathbf{X}) < 0$ and $p_k > 0$ if $g_k(\mathbf{X}) > 0$. Standard induction motors requirements are taken into consideration here, like the power factor and magnetizing current ratio, as well as rated torque design value (3.1). Great attention is also spent on the slot filling factor, high k_{fill} values make the stator slot manufacturing more difficult or even impossible, and also mean a worst slot equivalent thermal conductivity [18], leading to possible conductors heating and overtemperature.
The penalty functions and their weights are reported in the Tab. 5.2.

Name	**Optimization constraint**	**Function** g_k	**Weight** p_k
Power factor	$\cos\phi > 0.8$	$g_1 = \frac{0.8-\cos\phi}{\cos\phi}$	5
Magnetization current ratio	$\frac{I_\mu}{I_n} < 0.4$	$g_2 = \frac{\frac{I_\mu}{I_n}-0.4}{\frac{I_\mu}{I_n}}$	3
Nominal torque maximum	$T_n < 29\,\mathrm{Nm}$	$g_3 = \frac{T_n-29\,\mathrm{Nm}}{T_n}$	2
Nominal torque minimum	$T_n > 27\,\mathrm{Nm}$	$g_4 = \frac{27\,\mathrm{Nm}-T_n}{T_n}$	2
Slot filling factor	$k_{fill} < 0.45$	$g_5 = \frac{k_{fill}-0.45}{k_{[}fill}$	5

Table 5.2 – Penalty functions

Obviously, the population's individuals with the highest fitness raking will be considered the best ones and selected over the others.

5.3 Results

Different simulations have been carried out with different GA parameter combinations. For example, the population size N heavily affects the quality of the algorithm results and the computation time and, similarly, also does the crossover ratio CR. A relatively small population with high reproduction skills is chosen:

$$N = 30 \quad CR = 1.5 \quad p_c = 0.5 \quad p_m = 0.025 \tag{5.7}$$

As already said, the mutation probability is low to guarantee algorithm convergence. In this case, a good convergence is reached after 100 iterations (or generations).

5.3.1 Algorithm convergence and properties optimization

The evolution of the population through the generation is shown in the following figures. In Fig. 5.5–5.9, all individuals, i.e., motors, are represented using an x-y plot with their main dimensions: stack length and outer diameter. The best individual of each generation is underlined with the color red.

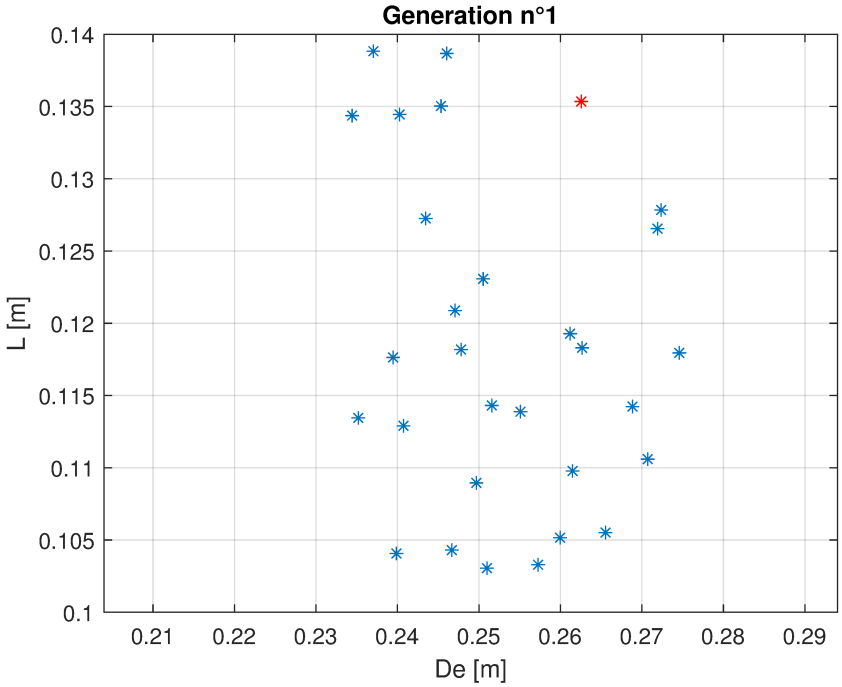

Figure 5.5 – Motors' main dimensions, first generation

The first motor's main dimensions, found previously, are in the center of the plot, so the GA suggests an optimized motor that is longer and with the same outer diameter. Nevertheless, a deep comparison between the basic IM and the optimized one will be carried out later. The convergence can be considered satisfying by the 100th generation since all individuals converge to a single point in the search space.

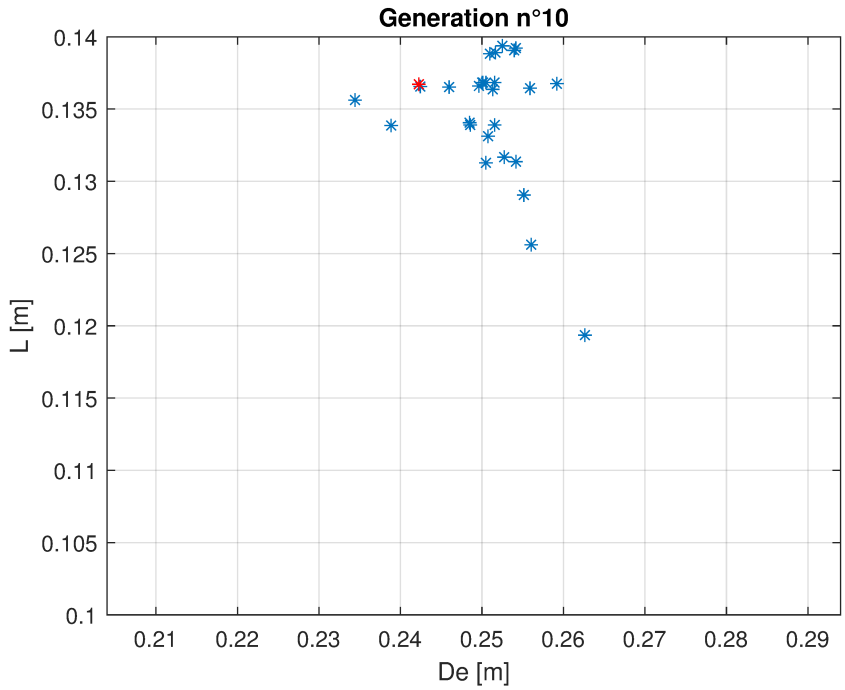

Figure 5.6 – Motors' main dimensions, 10th generation

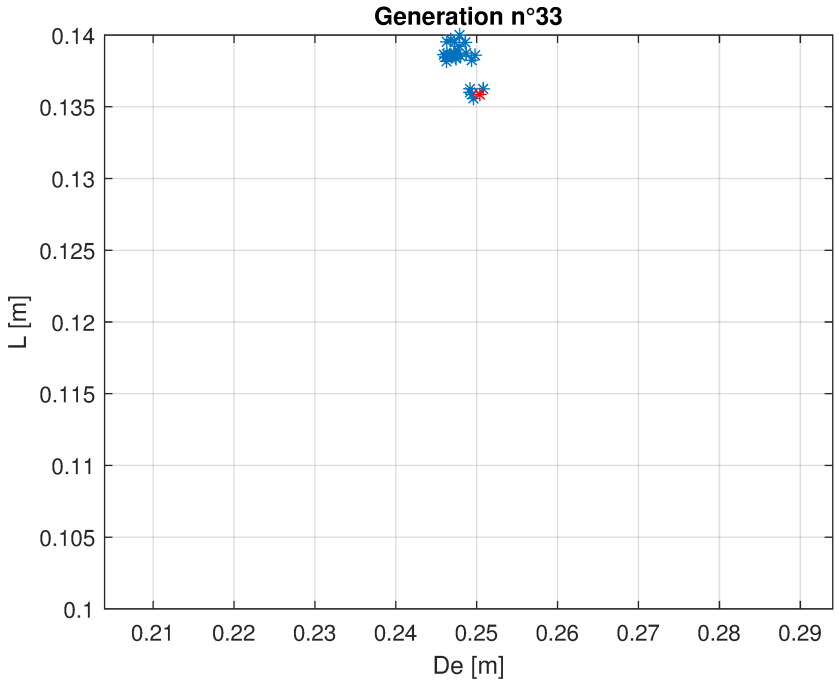

Figure 5.7 – Motors' main dimensions, 33rd generation

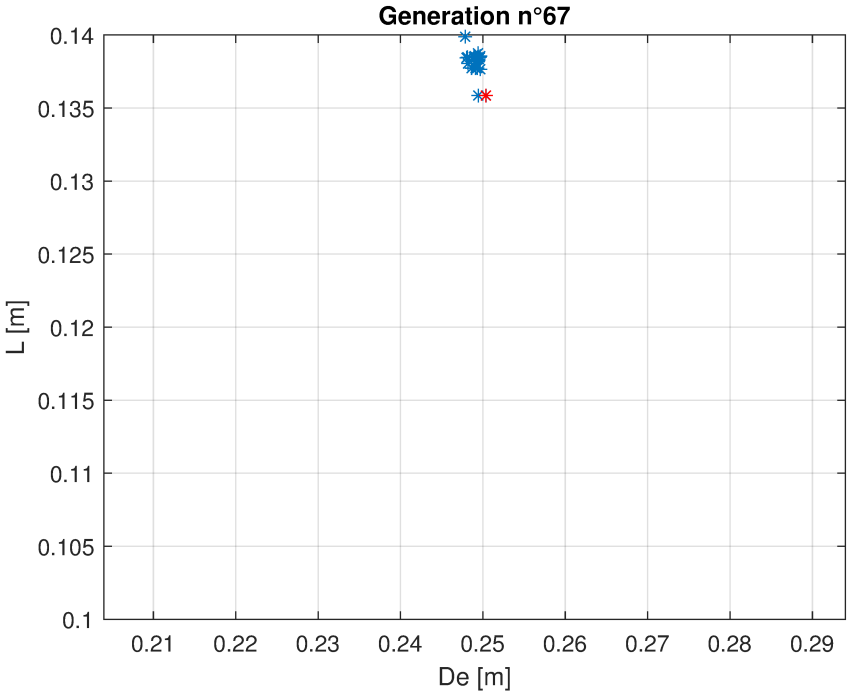

Figure 5.8 – Motors' main dimensions, 67th generation

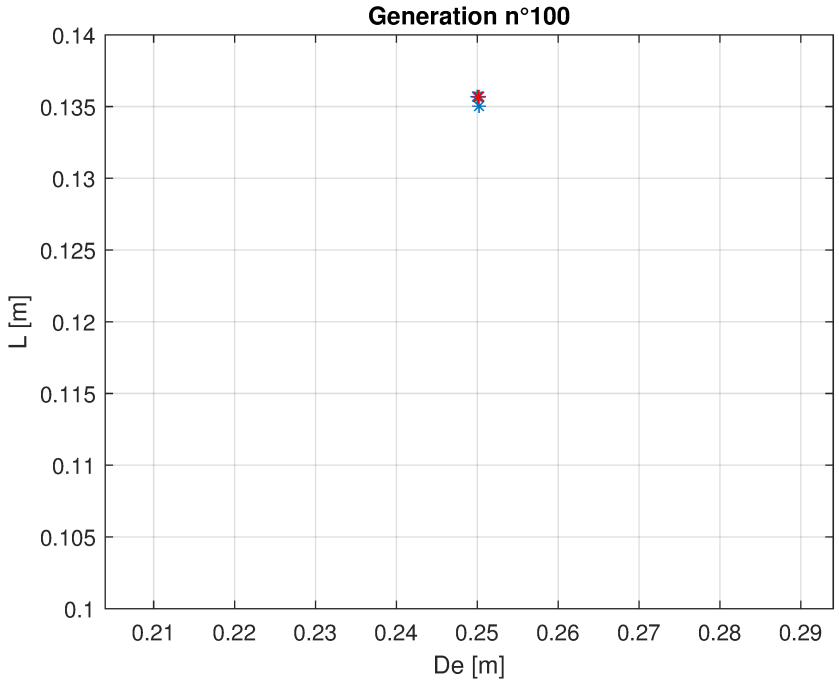

Figure 5.9 – Motors' main dimensions, 100th generation

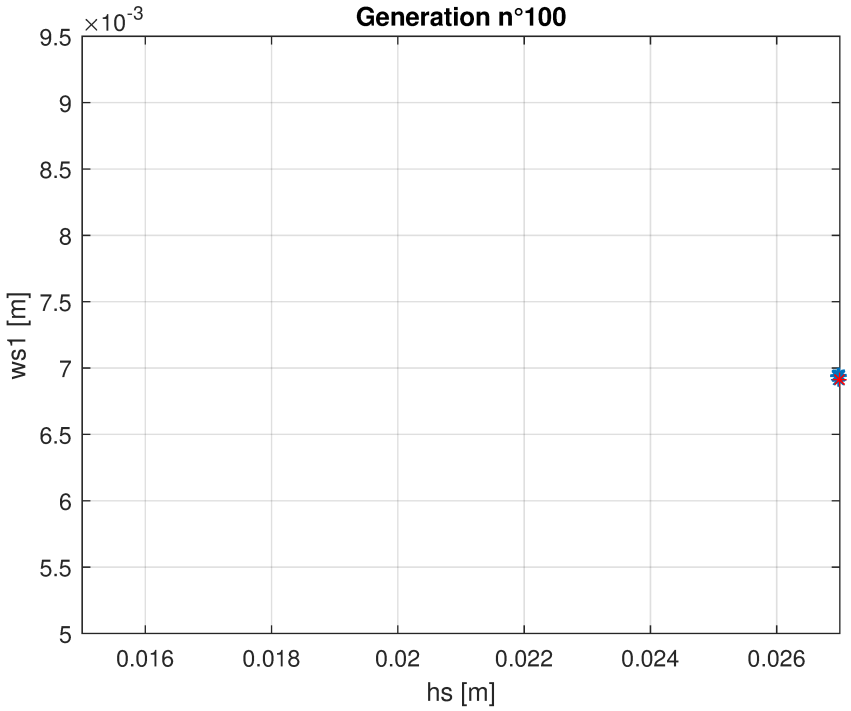

Figure 5.10 – Stator slot height and width, 100th generation

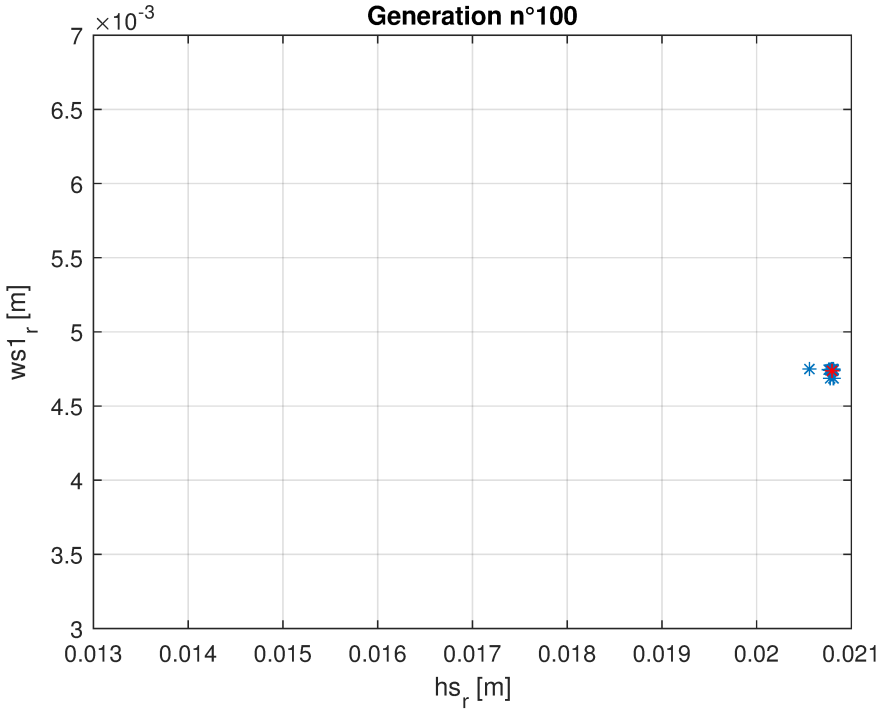

Figure 5.11 – Rotor slot height and width, 100th generation

The same convergence quality is shown plotting the population considering stator and rotor slot geometrical values, at the 100th generation (see Fig. 5.10 5.11).

As we see in the plots, the optimization suggests significantly higher stator and rotor slots.

Let's now consider the optimized motor characteristics. As stated in Sec. 5.2.2, this optimization aims to improve the efficiency while keeping the motor's weight under 50 kg and the winding relative temperature under 80 °C. The evolution of these main quantities during the GA execution is reported in Fig. 5.12.

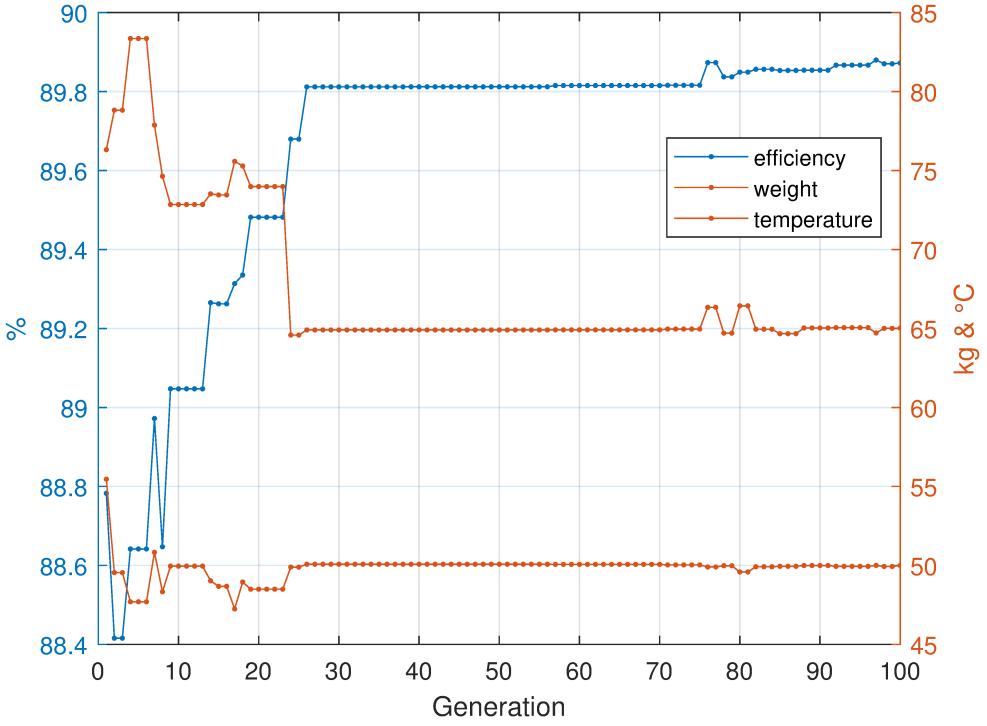

Figure 5.12 – Efficiency, weight, and winding temperature optimization

As a result, we can observe that the weight is almost constant around the target value, while the conductors' relative temperature is far more reduced. Usually, a weight reduction leads to a winding temperature increase; this can be explained by thinking that in a more compact motor, heat dissipation can be more difficult. The efficiency is continuously improved through the generations, reaching a more than acceptable final value close to 90%.

Furthermore, the fitness trend of the best individual and the generation average give us key information to quantify the optimization quality and convergence.
Considering a maximum fitness value of 30 (due to the weights w_k choice in the objective function, see Sec. 5.2.2), which means 100% efficiency and both weight and temperature target satisfied, in Fig. 5.13 a considerable fitness improvement occurs during the algorithm, which testifies the optimization quality.
On the other hand, the proximity between the best and average fitness, reached in the last generations, proves the convergence caliber of the algorithm since all individuals are really similar to the others.

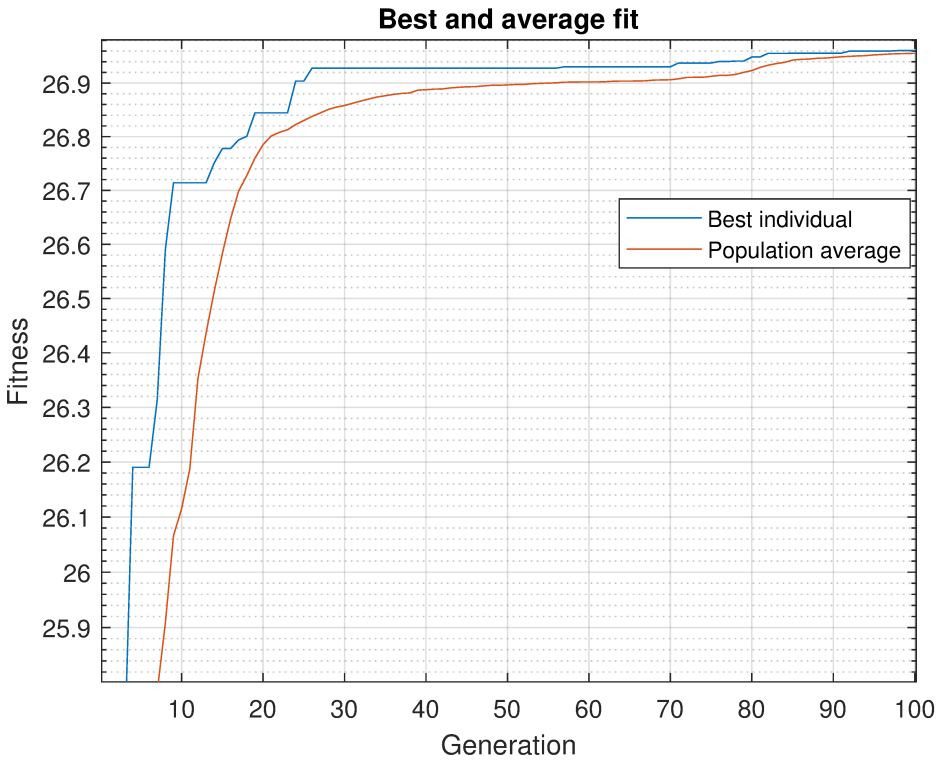

Figure 5.13 – Best and average fitness

5.3.2 Result comparison and discussion

A detailed comparison between the design parameters of the first designed motor and the optimized one is now presented in Tab. 5.3.

First of all, the GA solution suggests an IM with a smaller bore diameter and higher stack length, keeping the outer diameter identical to the original motor, thanks to weight and volume limitations.
Moreover, it may be worth noticing that the supply current density of the optimized motor is significantly lower than the first design value. This is reasonable considering the importance of the efficiency and winding overtemperature in the GA, which leads to preventing the stator copper losses minimizing the current density. As a result, the optimized stator slots are larger, mainly longer, to guarantee a proper slot-filling factor even with bigger cross-section conductors.
The rotor slots and short-circuit rings' dimensions are increased to maintain the induced current density and the rotor losses as low as possible.

Finally, looking at the expected motor's performances in Tab. 5.4, the GA made a remarkable difference in minimizing the estimated stator winding overtemperature, which was not considered in the first design process. The predicted relative temperature of the optimized motor certainly meets the reliability standards of this work, and it was achievable mainly by the stator current density limitation and a slight increase in the machine's weight and outer dimensions.

Variable	Symbol	Basic motor	Optimized motor
Bore diameter	D	140 mm	128.3 mm
Outer diameter	D_e	250 mm	250.1 mm
Stack length	L	120 mm	135.7 mm
Air gap	g	0.6 mm	0.505 mm
Supply current density	J	4.91 A/mm^2	3.08 A/mm^2
Back iron height	h_{bi}	34 mm	33.9 mm
Slot height	h_s	21 mm	27 mm
Slot wedge height	h_{wedge}	1.6 mm	1.4 mm
Slot width	w_{s1}	7.5 mm	6.9 mm
Rotor slot height	h_{sr}	17 mm	20.8 mm
Rotor slot wedge height	h_{wedge_r}	1.2 mm	0.91 mm
Rotor slot width	w_{s1r}	5 mm	4.7 mm
Rotor yoke diameter	D_y	33 mm	31.1 mm
Ring height	h_{ring}	17 mm	21 mm
Ring width	w_{ring}	15 mm	17.7 mm

Table 5.3 – Basic and optimized motor's design variable comparison

Property	Basic motor	Optimized motor	Unit
Efficiency	87.3	**89.9**	[%]
Weight	**42.9**	50.0	[kg]
Winding overtemperature	120.1	**65.0**	[°C]
Rated torque	28.4	28.5	[Nm]
Rated slip	2.76	2.01	[%]
Rated power factor	0.907	0.909	[-]
Slot-filling ratio	0.409	0.449	[-]
Air gap flux density	0.702	0.678	[T]
Stator tooth flux density	1.69	1.64	[T]
Rotor tooth flux density	1.72	1.71	[T]
Back iron flux density	1.52	1.35	[T]
Rotor yoke flux density	1.44	1.68	[T]
Magnetizing current ratio	39.9	**37.8**	[%]

Table 5.4 – Optimization results

Also, the final efficiency is significantly higher: considering the IEC/EN 60034-30-1 regulation for a 2-pole induction machine [9], the basic motor belongs to the IE1 (or Standard Efficiency) class, while the optimized one ends in the IE2 (or High Efficiency) class.
The rated torque, slip, and power factor are basically the same as the original IM. Only little changes in the flux density values in the magnetic circuit were found, especially in the back iron and the rotor yoke, due to the main geometrical parameters modification. Anyway, The GA solution does not dramatically differ from the starting one, which testifies to the optimization quality.

A graphical comparison between the original and optimized IM is shown in Fig. 5.14.

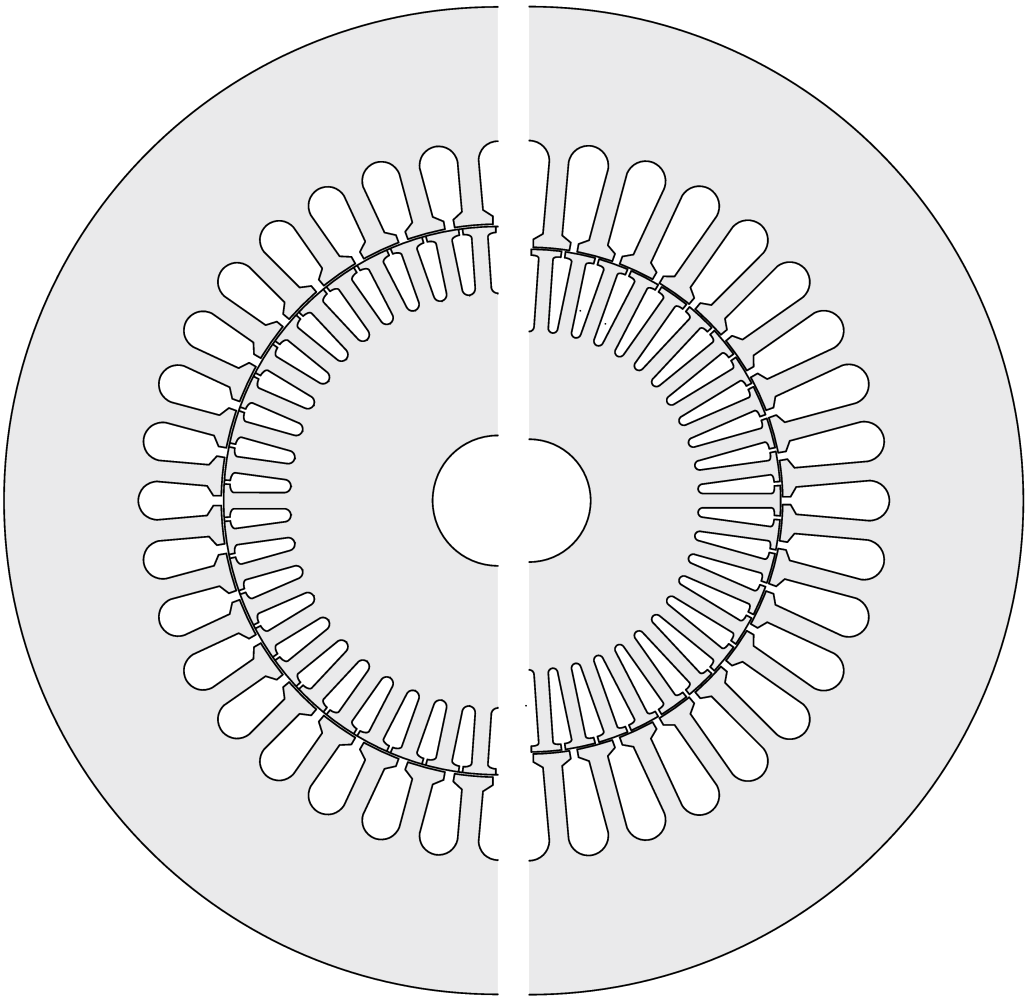

Figure 5.14 – Original (left) and optimized motor (right)

6 Finite Element Analysis

A Finite Element Analysis of the optimized motor carried out with the software F.E.M.M. is presented in this chapter. The simulations' computational cost is significantly high due to the complexity of the model and the non-linearity of the iron. So combining both analytical and FE models allows us to evaluate the IM's performances and parameters. As reported in [1], the flux lines are mainly 2-D lines, so a 2-D analysis is sufficient, saving computational time if compared with a full 3-D model. A 3-D correction is then needed to include end-winding and ring resistances and inductances, skewing effect, and so on.
The analysis performed follows the approach for the three-phase case shown in [1] and [3], extended to a nine-phase machine 6.1. The motor's parameters are evaluated by simulating

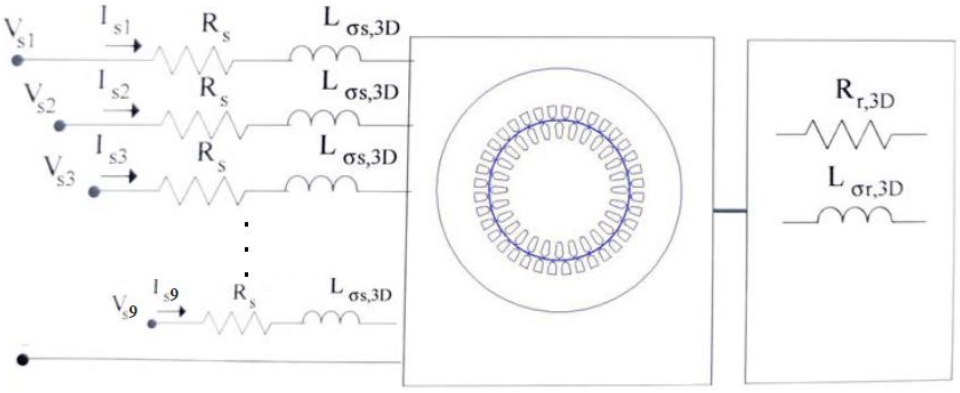

Figure 6.1 – FEM analysis scheme of the nine-phase machine

a no-load test and a locked rotor test, the equivalent circuit is then derived and used to determine the performances. Both simulations are carried out thanks to a MATLAB script, which builds the geometry, imposes the stator currents, and runs the post-process.

6.1 No-load simulation

The motor is analyzed in the rotor reference frame. This implies assuming a slip factor equal to zero, and also the relative frequency is equal to zero. So magnetostatic simulations are performed to investigate the iron saturation and evaluate the equivalent circuit parameters, such as the magnetizing inductance L_m.
The geometry is built and the material's properties are imposed: both copper and aluminum resistivity is calculated considering the winding operating temperature 5.3.1, the steel sheet is considered non-linear and its magnetization curve is copied by the datasheet [24]. The stator supply currents are imposed on each different phase as follows:

$$i_a = \sqrt{2} I_s \cos(0) \tag{6.1}$$

$$i_b = \sqrt{2} I_s \cos\left(-\frac{2}{9}\pi\right) \tag{6.2}$$

$$i_c = \sqrt{2} I_s \cos\left(-\frac{4}{9}\pi\right) \tag{6.3}$$

$$i_d = \sqrt{2} I_s \cos\left(-\frac{2}{3}\pi\right) \tag{6.4}$$

$$i_e = \sqrt{2} I_s \cos\left(-\frac{8}{9}\pi\right) \tag{6.5}$$

$$i_f = \sqrt{2} I_s \cos\left(-\frac{10}{9}\pi\right) \tag{6.6}$$

$$i_g = \sqrt{2} I_s \cos\left(-\frac{4}{3}\pi\right) \tag{6.7}$$

$$i_h = \sqrt{2} I_s \cos\left(-\frac{14}{9}\pi\right) \tag{6.8}$$

$$i_i = \sqrt{2} I_s \cos\left(-\frac{16}{9}\pi\right) \tag{6.9}$$

The result is shown in Fig. 6.2. Looking at the field lines and the currents set above, we can

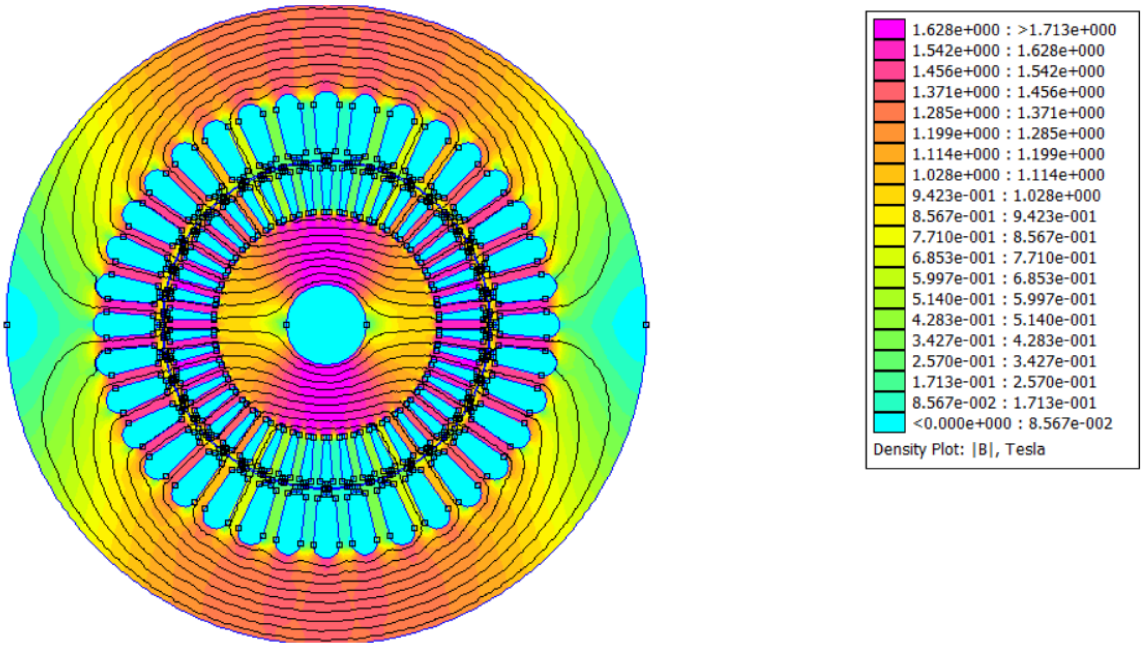

Figure 6.2 – Flux density plot, no-load test

see that the phase a magnetic axis is horizontal, as expected.

The magnetizing inductance can now be determined with three different methods [3]:

- using the linkage fluxes. Using F.E.M.M. post-processing, the flux linkage of the a-phase can be computed by performing the magnetic vector potential integral over the stator slots:

$$\Lambda_a = n_{cs} \frac{1}{S_{slot}} \sum_{q=1}^{Q} k_{aq} \int_{S_{slot}} A_z dS \tag{6.10}$$

where k_{aq} is the slot coefficient for the a-phase in the slot matrix 2.3.2. The magnetizing inductance is then given:

$$L_m = \frac{\Lambda_a}{\sqrt{2} I_s} \tag{6.11}$$

- using the magnetic energy W, integrated over the motor region.

$$L_m = \frac{4}{9} \frac{W}{(\sqrt{2} I_s)^2} \tag{6.12}$$

This formulation is valid only in linear conditions so without saturation in the iron.

- using the integral $\int A_z \times J \, dS$ over the motor region.

$$L_m = \frac{2}{9} \frac{W_{AJ}}{(\sqrt{2} I_s)^2} \tag{6.13}$$

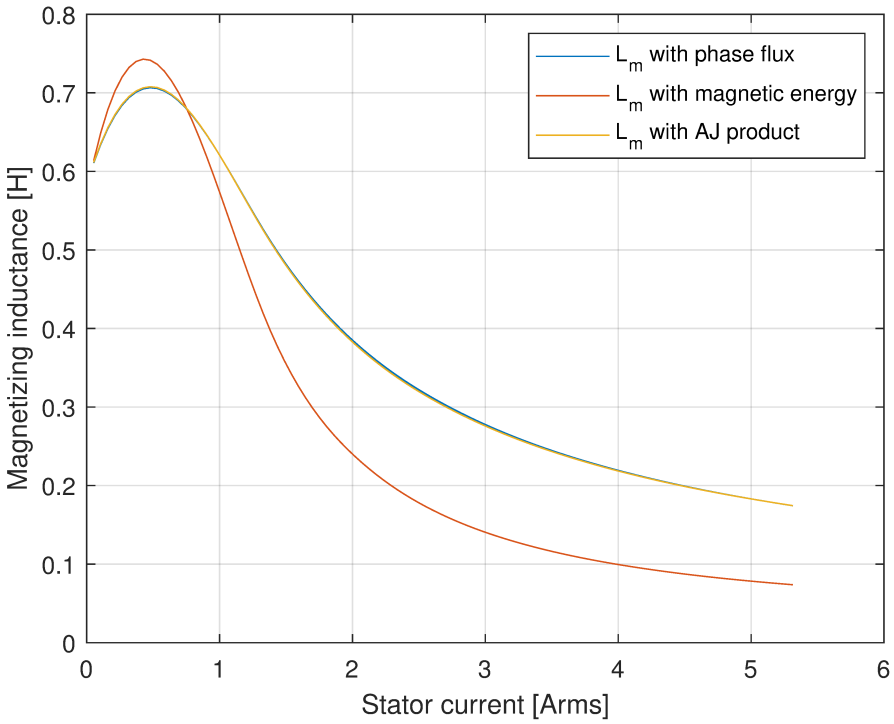

Figure 6.3 – Magnetizing inductance over stator current

The magnetizing inductance is calculated with these three different methods, varying the stator current value. As we can see in Fig.6.5, linkage flux and W_{AJ} methods are equivalent and close to the magnetic energy only for low current values when the problem is still linear. The magnetizing inductance at the nominal current value is $L_m = 0.385\,\mathrm{H}$.

Draw the magnetization curve 6.5 of the machine is also possible thanks to linkage flux:

$$U = \omega \, \Lambda \tag{6.14}$$

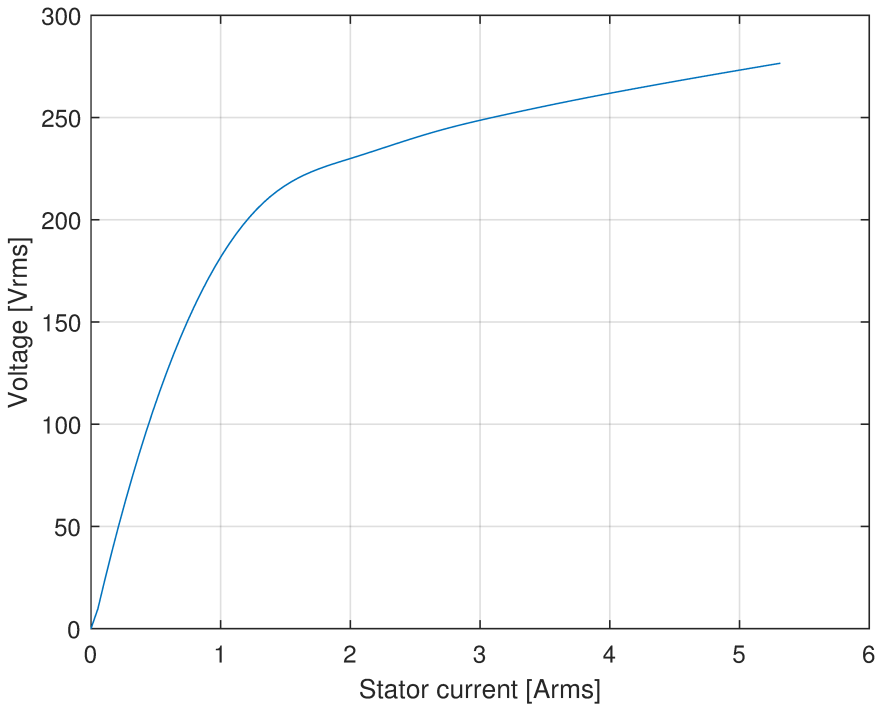

Figure 6.4 – Magnetization curve

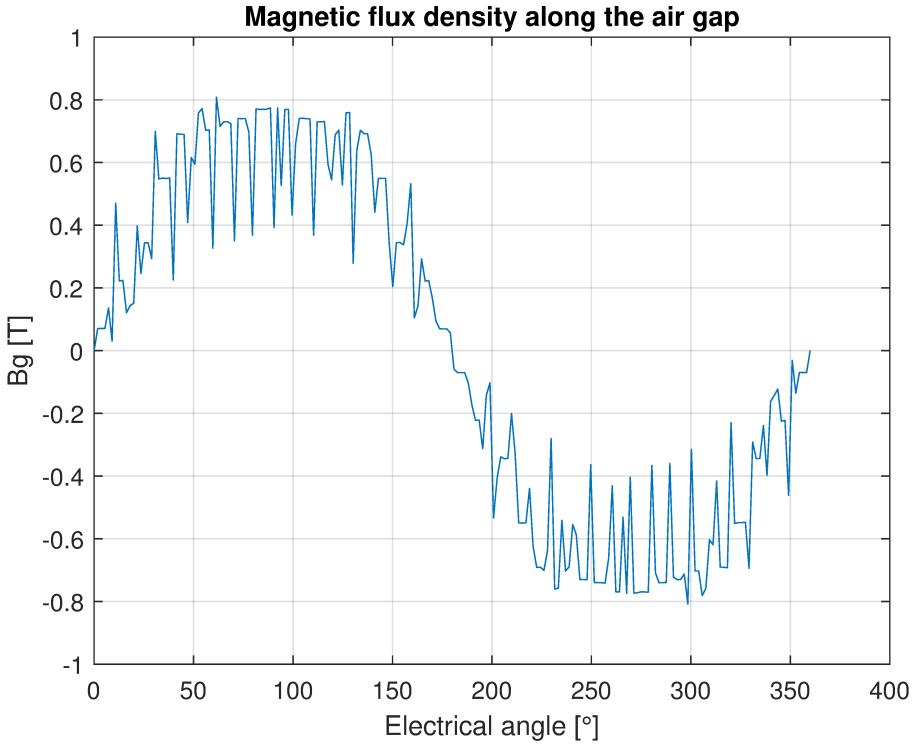

Figure 6.5 – Bg along the air gap with $I_S = I_\mu$

Knowing the supply voltage $U = 230\,\mathrm{V}$ the magnetizing current is given $I_\mu = 2\,\mathrm{A}$, with a magnetizing current ratio of 37.6% as expected in the design process 5.3.2.

The magnetic flux density along the air gap, imposing the magnetizing current as stator current, is presented in Fig.6.5. The fundamental's peak is really close to $B_g = 0.678\,\mathrm{T}$ stated in 5.3.2.

6.2 Locked rotor simulation

The locked rotor simulation is a magneto-dynamic analysis that allows us to determine the rotor resistance R_{r2D} and the rotor leakage inductance $L_{\sigma r2D}$, depending on the rotor frequency. Since the rotor is locked, its relative frequency is equal to the supply and the simulation's frequency.
Therefore the following imaginary set of currents is imposed along the stator winding with

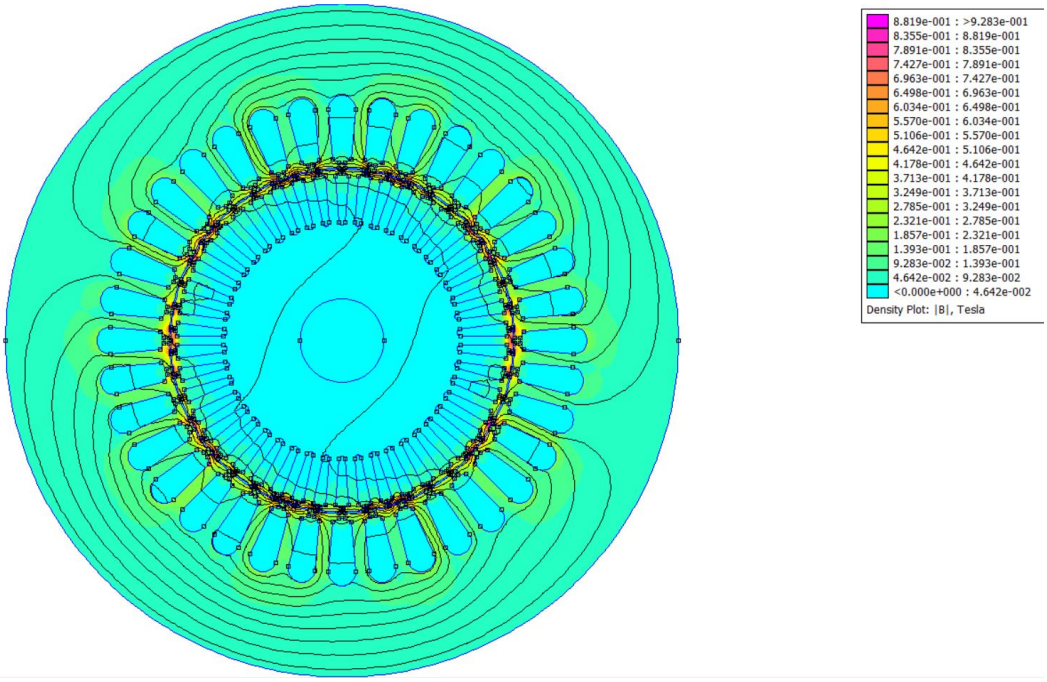

Figure 6.6 – Flux density plot, locked rotor test

different frequency values between zero and 50 Hz:

$$i_a = \sqrt{2} I_n \left(\cos\left(0\right) + i \sin\left(0\right)\right) \tag{6.15}$$

$$i_b = \sqrt{2} I_n \left(\cos\left(-\frac{2}{9}\pi\right) + i \sin\left(-\frac{2}{9}\pi\right)\right) \tag{6.16}$$

$$i_c = \sqrt{2} I_n \left(\cos\left(-\frac{4}{9}\pi\right) + i \sin\left(-\frac{4}{9}\pi\right)\right) \tag{6.17}$$

$$i_d = \sqrt{2} I_n \left(\cos\left(-\frac{2}{3}\pi\right) + i \sin\left(-\frac{2}{3}\pi\right)\right) \tag{6.18}$$

$$i_e = \sqrt{2} I_n \left(\cos\left(-\frac{8}{9}\pi\right) + i \sin\left(-\frac{8}{9}\pi\right) \right) \tag{6.19}$$

$$i_f = \sqrt{2} I_n \left(\cos\left(-\frac{10}{9}\pi\right) + i \sin\left(-\frac{10}{9}\pi\right) \right) \tag{6.20}$$

$$i_g = \sqrt{2} I_n \left(\cos\left(-\frac{4}{3}\pi\right) + i \sin\left(-\frac{4}{3}\pi\right) \right) \tag{6.21}$$

$$i_h = \sqrt{2} I_n \left(\cos\left(-\frac{14}{9}\pi\right) + i \sin\left(-\frac{14}{9}\pi\right) \right) \tag{6.22}$$

$$i_i = \sqrt{2} I_n \left(\cos\left(-\frac{16}{9}\pi\right) + i \sin\left(-\frac{16}{9}\pi\right) \right) \tag{6.23}$$

In Fig. 6.6 the FEA output. It can be noticed that the flux lines do not enter the rotor so easily with respect to the no-load test.
Thanks to F.E.M.M. post-processing, the following useful data can be obtained: the magnetic energy W, the rotor Joule losses P_{jr}, and the torque acting on the rotor by using Maxwell's stress tensor. The rotor can be described using a single-phase equivalent circuit 6.7, in which the equivalent resistance and inductance (second picture of Fig. 6.7) can be derived [1]:

$$R_{eq} = \frac{2 P_{jr}}{9 I_n^2} \tag{6.24}$$

$$L_{eq} = \frac{4}{9} \frac{W}{I_n^2} \tag{6.25}$$

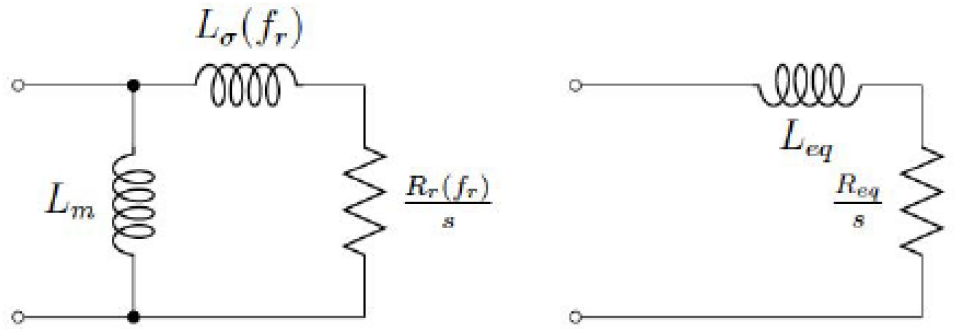

Figure 6.7 – Rotor equivalent circuit under locked rotor operation [1]

The other single-phase equivalent circuit parameters, such as the rotor resistance R_r and inductance L_σ (first picture of Fig. 6.7), are calculated as a function of the frequency from the equivalent parameters and the magnetizing inductance L_m, which is constant and already calculated in the no-load simulation:

$$R_r(f_r) = \frac{L_m^2 R_{eq}}{(\frac{R_{eq}}{\omega})^2 + (L_m - L_{eq})^2} \tag{6.26}$$

$$L_\sigma(f_r) = L_m \frac{L_{eq}(L_m - L_{eq}) - (\frac{R_{eq}}{\omega})^2}{(\frac{R_{eq}}{\omega})^2 + (L_m - L_{eq})^2} \tag{6.27}$$

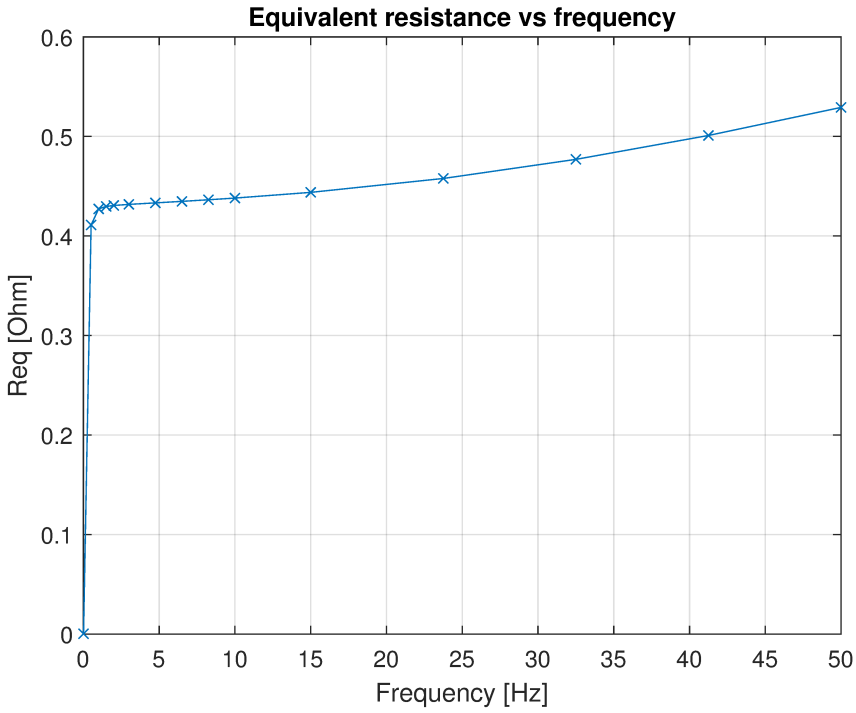

Figure 6.8 – Rotor equivalent resistance over frequency

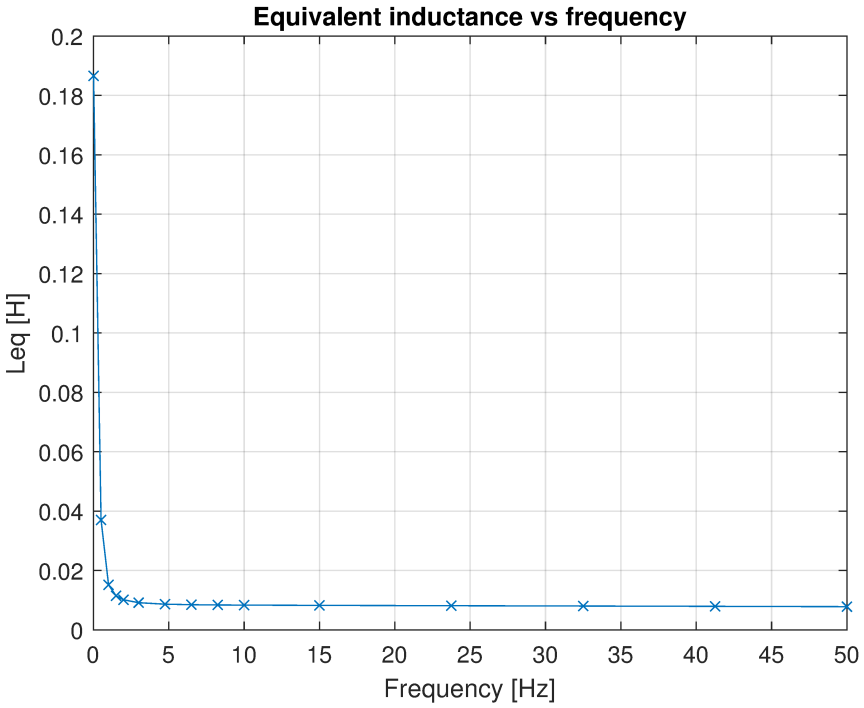

Figure 6.9 – Rotor equivalent inductance over frequency

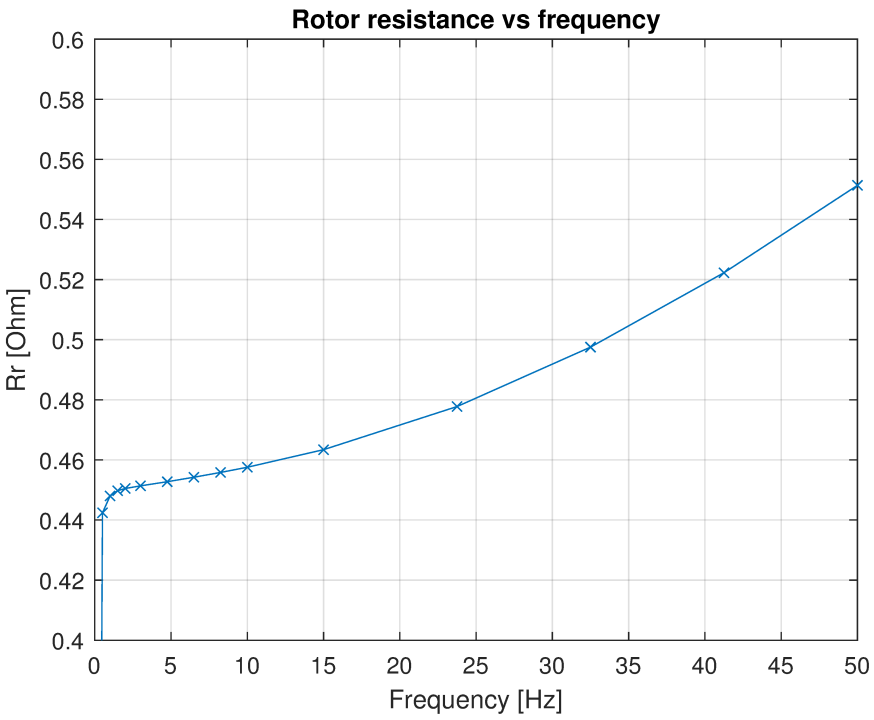

Figure 6.10 – Rotor resistance over frequency

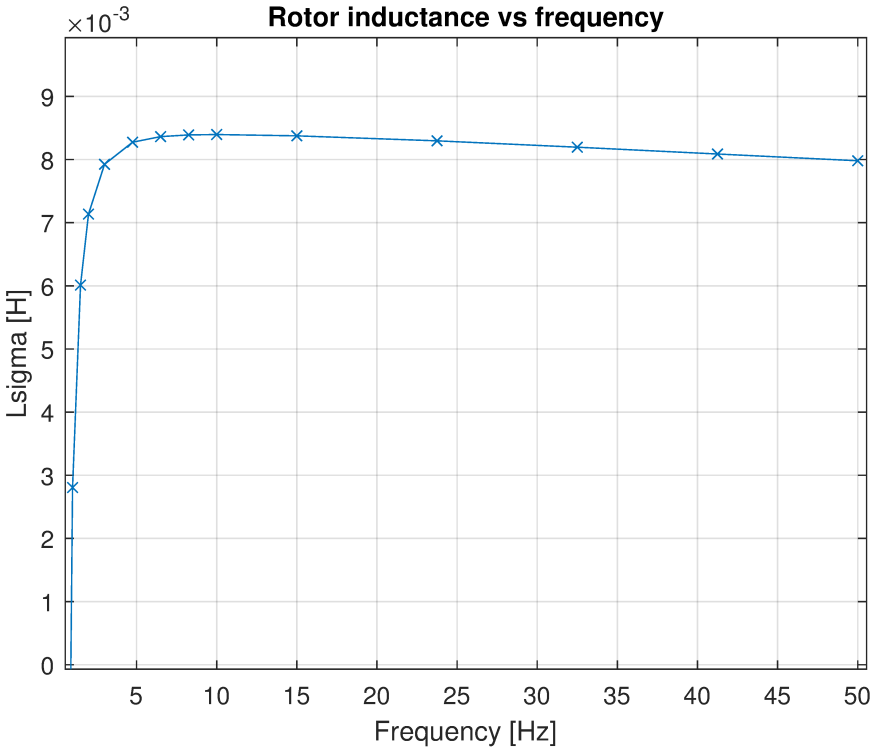

Figure 6.11 – Rotor inductance over frequency

Finally, also the torque T acting on the locked rotor over different frequencies is evaluated with two different methods:

- with Maxwell's stress tensor, which is directly given by F.E.M.M. post-processing
- with the rotor Joule losses P_{jr} since $T = P_{jr}\frac{p}{2\pi f}$

The result is shown in Fig. 6.12.

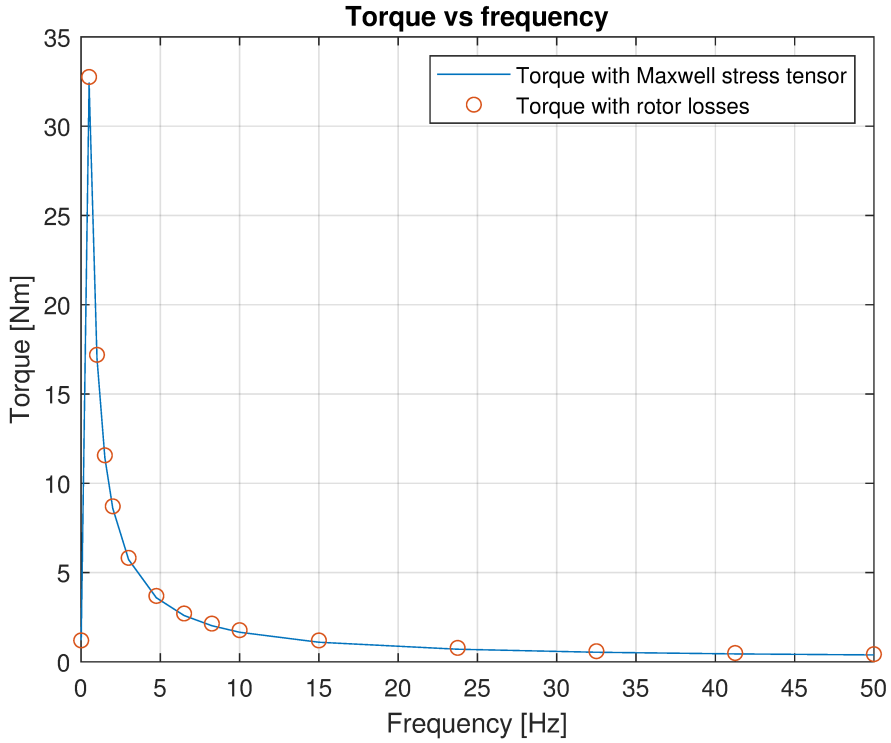

Figure 6.12 – Torque over frequency

It is worth mentioning that the trend reported in Fig. 6.12 is not the mechanical characteristic of the machine, but is the torque acting on the rotor at nominal current calculated at different frequencies. The motor nominal torque can be extrapolated knowing the nominal slip, and consequently the nominal rotor relative frequency. This value is really close to the GA output 5.3.2, as will be described in the following section.

6.3 Performance

In order to determine all the parameters of the equivalent circuit, it is necessary to take into consideration also the three-dimensional elements such as the end-winding and short-circuit rings, that do not take place in the previously described simulation. These corrections are

done analytically. The short-circuit rings' resistance must be added to the rotor resistance, according to [1]:

$$K_{ring} = \frac{2}{\pi} \frac{Q_r}{2p^2} \frac{D_r}{L} \frac{S_{bar}}{h_{ring}\, w_{ring}} \tag{6.28}$$

So, the rotor resistance as a function of the frequency is corrected as follows:

$$R_r(f_r) = R_{r2D}(f_r)\,(1 + K_{ring}) \tag{6.29}$$

The leakage inductance is corrected as well, considering the short-circuit rings and rotor skewing [1]:

$$L_{\sigma ring} = \mu_0\, k_r \left(\frac{K_w}{K_{skew}}\right)^2 q^2 \frac{\pi D_r}{L} \tag{6.30}$$

where $k_r = 0.36$ if $2p = 2$, whereas $k_r = 0.18$ if $2p > 2$.
The total rotor leakage inductance is now given:

$$L_{\sigma r} = L_{\sigma r2D} + L_{\sigma ring} + L_{\sigma skew} \tag{6.31}$$

It is now possible to reconstruct the IM equivalent circuit 6.13, evaluating the stator quantities as already done in Sec. 4.4. Solving the circuit as already done in Sec.4.4 a nominal slip

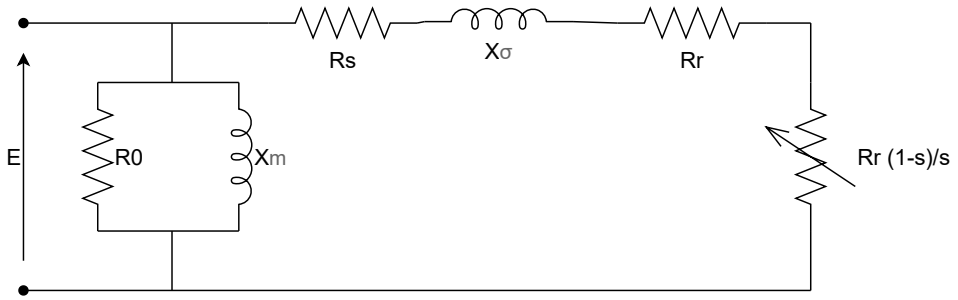

Figure 6.13 – Simplified equivalent circuit

of $s_n = 2.5\%$ is found, corresponding to a nominal torque of $T_n = 28$Nm, a nominal power factor of $\cos\phi_n = 0.906$, and a nominal efficiency of $\eta_n = 89.2\%$ which are acceptable values considering the analytical GA results (see Sec. 5.3.2).
The plots of the main quantities, varying the rotor slip, i.e. its velocity, are reported below.

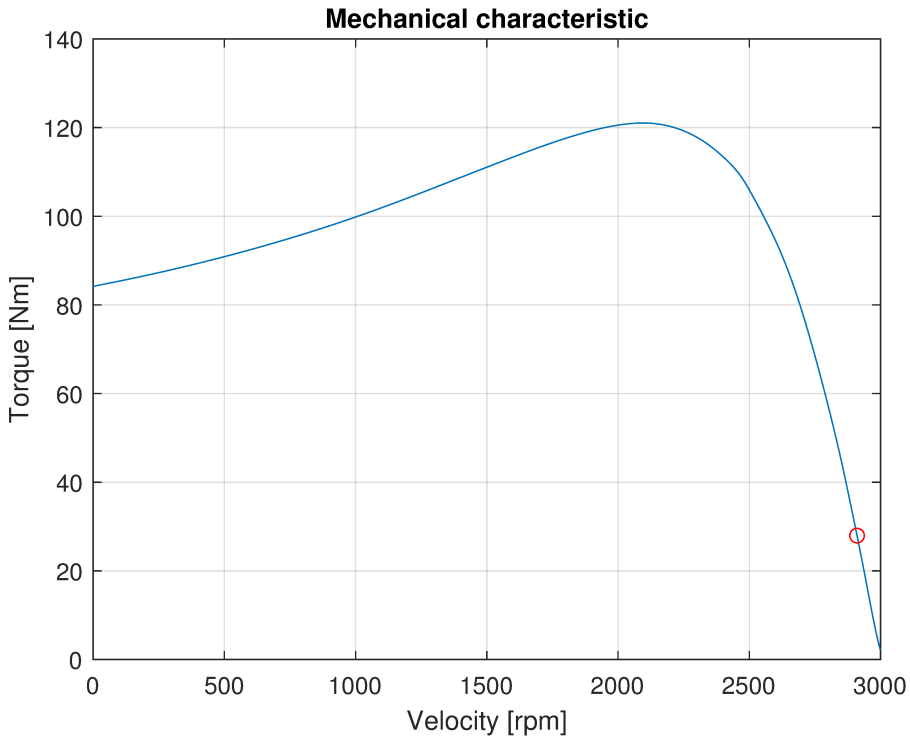

Figure 6.14 – Mechanical characteristic

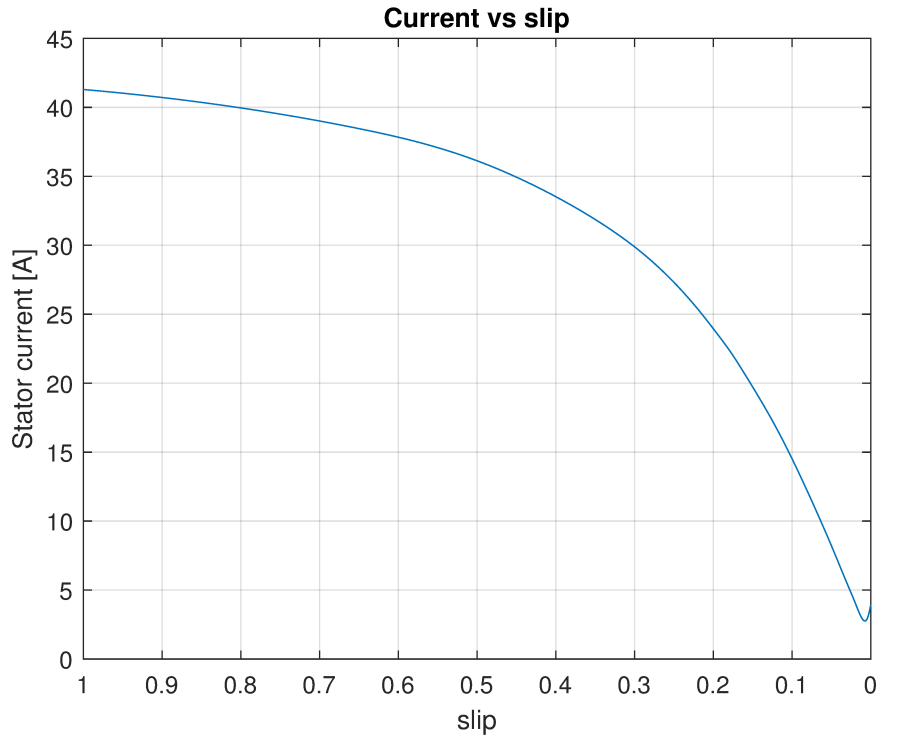

Figure 6.15 – Current - slip characteristic

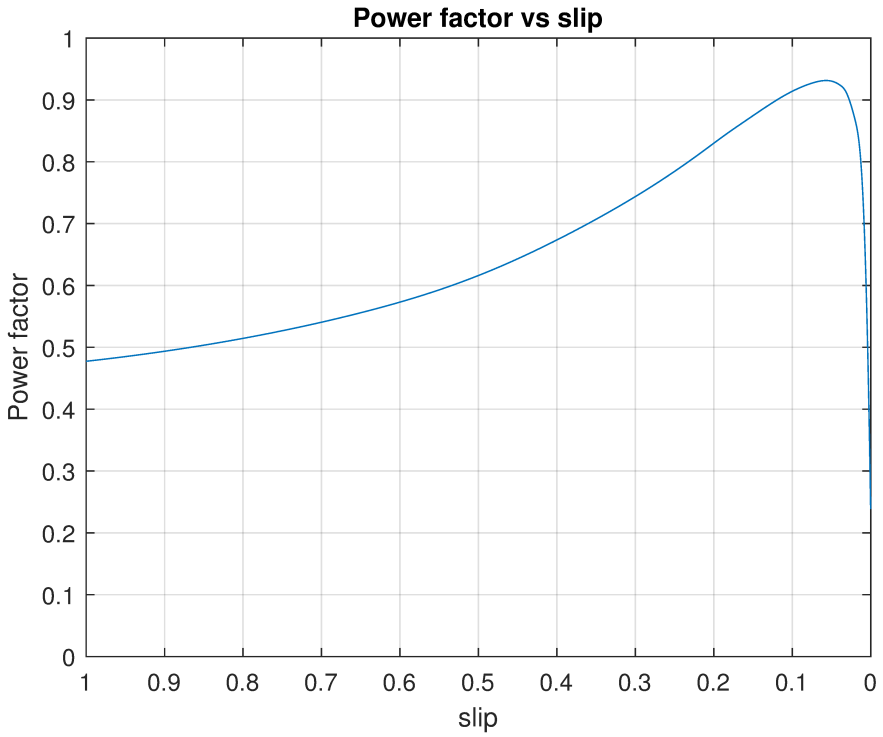

Figure 6.16 – Power factor - slip characteristic

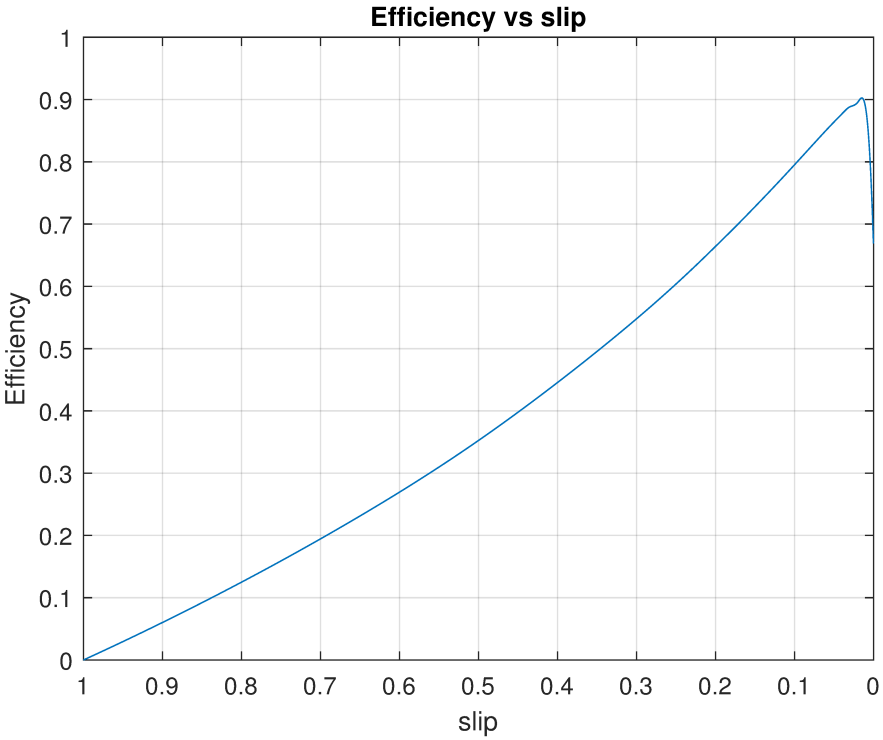

Figure 6.17 – Efficiency - slip characteristic

7 Conclusion and outlook

The increase in electric transportation leads to higher standards for electric machines' reliability and fault tolerance. Indeed, much research and development has been spent studying multi-phase machines, which can provide those standards more easily than the common three-phase ones [12].
In this work, a 9-phase induction motor is been designed and analyzed as an alternative to well-known PM motors, already commonly studied. The asynchronous motor is cheaper since no permanent magnets are present, and can also meet good performances.

First, a distributed winding is chosen to guarantee the best MMF distribution over the air gap to reduce harmonics as much as possible. This leads to selecting the configuration with 2 poles and 36 stator slots. The proposed winding is then analyzed, as well as its harmonic content. Secondly, the motor is analytically designed following empirical and commonly used formulas in literature.
In the following chapters, the motor is optimized through a genetic algorithm to achieve optimum values of efficiency, weight, and winding temperature, with satisfying results. Finally, its performances are determined using F.E.M.M. software to check analytical calculations, with good results. All main optimized IM's characteristics and performances are evaluated thanks to a more precise equivalent circuit built from the Finite Element Analysis.
The final optimized IM proposed presents a bore diameter $D = 128.3\,\text{mm}$, an outer diameter $D_e = 250.1\,\text{mm}$, and a total length $L = 135.7\,\text{mm}$, with a rated torque $T = 28.5\text{Nm}$ and a rated efficiency $\eta = 89.9\%$.
Comparing it to the starting PM motor proposed in [22], similar geometrical values are found but the IM presents a lower-rated torque, as expected.

The possible further developments about the topic under investigation could be building a first test bench prototype to validate the analytical calculations and the design of a proper control strategy that ensures the operation under fault conditions to achieve a high level of reliability.

I trust this work could help the progress of more reliable and safe electric transportation, breaking the standards in electric machine design and concept, and always looking for new unthinkable applications.

Ringraziamenti

Trovo quanto mai doveroso concedermi l'uso dell'Italiano per esprimere i ringraziamenti. Premettendo che più della metà di questa tesi è stata concepita e scritta in una stanza di ospedale, viene naturale ringraziare medici, infermieri e personale che stanno contribuendo al lungo e difficoltoso percorso di guarigione.

Un sentito pensiero di gratitudine va al professor Bianchi, per avermi permesso di lavorare su un tema per me molto interessante e per la vicinanza dimostrata in questi mesi; così come al professor Kammermann sempre disponibile e comprensivo.

A tutti coloro che, seppur a distanza, mi sono stati vicini, troppi da nominare.

Un ringraziamento che può sembrare scontato ma non lo è, va ai miei genitori. Per tutti i consigli e il supporto durente gli anni di università e in particolare per i sacrifici fatti e l'unità perpetua e indissolubile che li contraddistingue anche durante questo ultimo periodo di difficoltà.

Infine a te, che quasi in contemporanea con l'inizio di questa tesi sei arrivata stile manzoniana provvidenza e non te ne sei più andata. Perchè abbiamo affrontato troppo in troppo poco tempo e nonostante tutto tu sei lì a darmi forza e farmi sentire vivo anche quando ne dubito. Seppur architetto una parte di questa tesi in ingegneria è anche tua.

A Appendix

A.1 Slot coefficient calculation

The constant k_{slot} evaluation is based on the slot's geometry and conductors' position.
Taking for example the stator slot and assuming that the conductors take place only in the

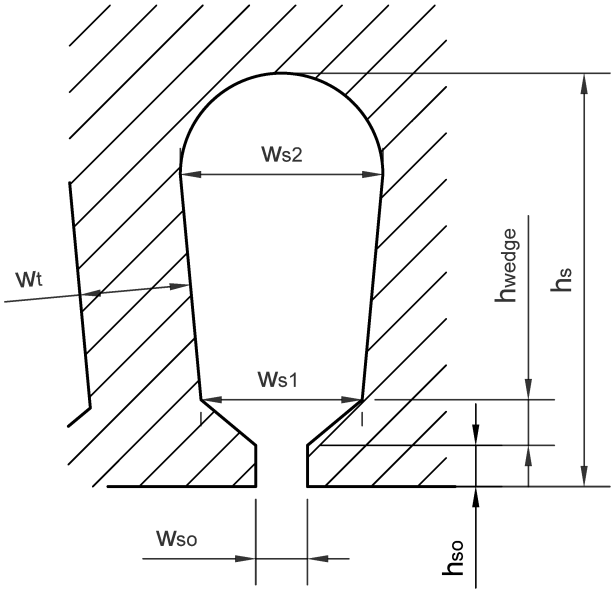

Figure A.1 – Stator slot

main part of the slot, the following formula is used [5]:

$$k_{slot} = \frac{h_s o}{w_s o} + \frac{h_{wedge}}{w_{s1} - w_{so}} \ln \frac{w_{s1}}{w_{so}} + \frac{h_s - h_{so} - h_{wedge}}{w_{s2}} \frac{\beta^2 - \beta^4/4 - \ln \beta - 3/4}{(1-\beta)(1-\beta^2)^2} \tag{A.1}$$

where $\beta = \frac{w_{s1}}{w_{s2}}$

A.2 High-order harmonics coefficient

In the figure, the correlation between the belt constant and the number of poles and slots. In our case, since q_p is high, the belt constant is low and can be considered equal to 1.

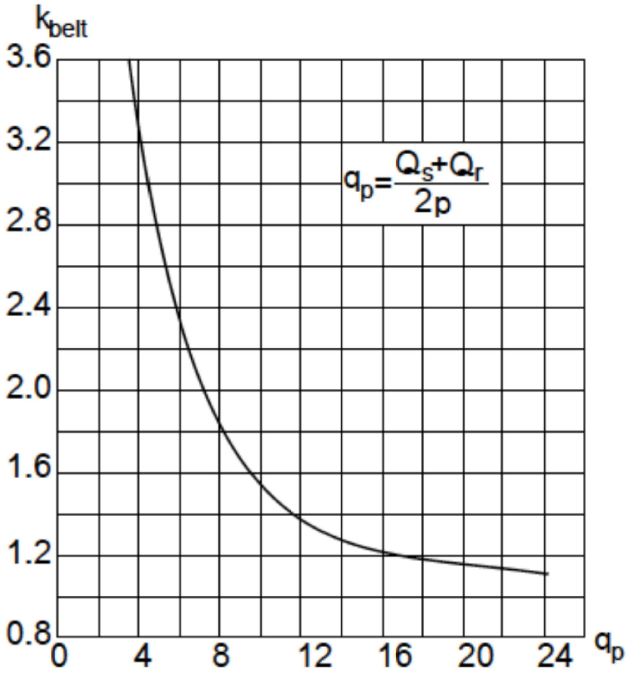

Figure A.2 – K_{belt} constant [5]

Bibliography

[1] Alberti, L.; Bianchi, N.; Bolognani, S.: "A Very Rapid Prediction of IM Performance Combining Analytical and Finite-Element Analysis". In: *IEEE Transactions on Industry Applications* 44.5 (2008), pp. 1505–1512. DOI: 10.1109/TIA.2008.2002185.

[2] Andriollo, M.; Martinelli, G.; Morini, A.: *Macchine elettriche rotanti*. Cortina editore, 2003.

[3] Bianchi, N.: *Calcolo delle macchine elettriche col metodo degli elementi finiti*. Cleup, 2001.

[4] Bianchi, N.; Bolognani, S.: "Design optimisation of electric motors by genetic algorithms". In: *IEE Proceedings - Electric Power Applications* 145 (Sept. 1998), pp. 475–486. DOI: 10.1049/ip-epa:19982166.

[5] Bianchi, N.; Bolognani, S.: *Metodologie di progettazione delle macchine elettriche*. Cleup, 2000.

[6] Cassoret, B.; Lecointe, J.-P.; Brudny, J.-F.: "Influence of the Pole Number on the Magnetic Noise of Electrical AC Machines". In: *Progress In Electromagnetics Research B* 33 (Jan. 2011), pp. 83–97. DOI: 10.2528/PIERB1106200.

[7] Cunkas, M.; Akkaya, R.: "Design Optimization of Induction Motor by Genetic Algorithm and Comparison with Existing Motor". In: *Mathematical and Computational Applications* 11 (Dec. 2006). DOI: 10.3390/mca11020193.

[8] Ferreira, F. J. T. E.; Baoming, G.; Almeida, A. T. de: "Reliability and Operation of High-Efficiency Induction Motors". In: *IEEE Transactions on Industry Applications* 52.6 (2016), pp. 4628–4637. DOI: 10.1109/TIA.2016.2600677.

[9] *IEC IM efficiecy classes*. URL: https://www.iec.ch/government-regulators/electric-motors.

[10] *IEC insulation class explanation - Regal Beloit*. URL: www.regalbeloit.eu (visited on 11/01/2023).

[11] Joksimović, G. M.; Riger, J.; Wolbank, T. M., ; et al.: "Stator-Current Spectrum Signature of Healthy Cage Rotor Induction Machines". In: *IEEE Transactions on Industrial Electronics* 60.9 (2013), pp. 4025–4033. DOI: 10.1109/TIE.2012.2236995.

[12] Kammermann, J.; Bolvashenkov, I.; Herzog, H.-G.: "Improvement of Reliability and Fault Tolerance of Traction Drives by Means of Multiphase Actuators". In: *Drive Systems 2017; 7th VDE/VDI Symposium*. 2017, pp. 1–6.

[13] Kammermann, J.; Bolvashenkov, I.; Ugalde, J. L., ; et al.: "Choice of Phase Number for a Multiphase Traction Motor to Meet Requirements on Fault Tolerance". In: *2019 International Conference on Electrotechnical Complexes and Systems (ICOECS)*. 2019, pp. 1–6. DOI: 10.1109/ICOECS46375.2019.8949960.

[14] Laksar, J.; Cermak, R.; Hruska, K.: "Challenges in the Electromagnetic Design of Multiphase Machines: Winding and Equivalent Circuit Parameters". In: *Energies* 14.21 (2021).

[15] Lambora, A.; Gupta, K.; Chopra, K.: "Genetic Algorithm- A Literature Review". In: *2019 International Conference on Machine Learning, Big Data, Cloud and Parallel Computing (COMITCon)*. 2019, pp. 380–384. DOI: 10.1109/COMITCon.2019.8862255.

[16] Levi, E.: "Multiphase Electric Machines for Variable-Speed Applications". In: *IEEE Transactions on Industrial Electronics* 55.5 (2008), pp. 1893–1909.

[17] Moros, O.; Richnow, J.; Gerling, D.: "New Cost Effective Concentrated Winding Topology for Induction Machines". In: 2014.

[18] Popescu, M.; Dorrell, D. G.; Alberti, L., ; et al.: "Thermal analysis of duplex 3-phase induction motor under fault operating conditions". In: *2012 XXth International Conference on Electrical Machines*. 2012, pp. 1875–1881. DOI: 10.1109/ICElMach.2012.6350137.

[19] Pyrhoenen, J.; Jokinen, T.; Hrabovcovà, V.: *Design of Rotating Electrical Machines*. John Wiley & Sons, 2008.

[20] El-Refaie, A. M.; Shah, M. R.: "Comparison of Induction Machine Performance with Distributed and Fractional-Slot Concentrated Windings". In: *2008 IEEE Industry Applications Society Annual Meeting*. 2008, pp. 1–8.

[21] Shen, Y.; Zhu, C.; Wang, X.: "Slot Optimization Design of Induction Motor for Electric Vehicle". In: *IOP Conference Series: Materials Science and Engineering* 301 (Jan. 2018), p. 012081. DOI: 10.1088/1757-899X/301/1/012081.

[22] Tippe, L.; Kammermann, J.; Bolvashenkov, I., ; et al.: "Concept Analysis and Design of a 9-Phase Permanent Magnet Synchronous Machine". In: *2018 AEIT International Annual Conference*. 2018, pp. 1–6. DOI: 10.23919/AEIT.2018.8577431.

[23] *Types of leakage flux*. URL: https://www.eeeguide.com/types-of-magnetic-leakage-flux-in-induction-motor/.

[24] *Voestalpine - isovac 350-50 A*. URL: https://www.voestalpine.com/division_stahl/content/download/32782/347314/file/DB_isovac_350-50A_E_280715.pdf (visited on 11/10/2022).

[25] Williamson, S.; Smith, S.: "Pulsating torque and losses in multiphase induction machines". In: *Conference Record of the 2001 IEEE Industry Applications Conference. 36th IAS Annual Meeting (Cat. No.01CH37248)*. Vol. 2. 2001, 1155–1162 vol.2.